Department of Physics and Astronomy

University of Heidelberg

Master thesis

in Physics

submitted by

Caren Kresse

born in Tettnang (Germany)

**2017**

# Track Reconstruction of Photon Conversion Electrons from Displaced Vertices in the Mu3e Detector

This Master thesis has been carried out by

Caren Kresse

at the

Physikalisches Institut der Universität Heidelberg

under the supervision of

Prof. Dr. André Schöning

**Track Reconstruction of Photon Conversion Electrons in the *Mu3e* Detector**

The *Mu3e* collaboration is searching for the lepton flavor violating decay $\mu^+ \to e^+e^-e^+$ with a detector based on thin silicon pixel sensors. With a minimized material budget to reduce multiple Coulomb scattering, it is optimized for reconstructing low momentum electrons with high precision. Therefore, the detector can also be used to search for New Physics phenomena in other rare processes in the low energy range, or to perform precision measurements. Many of these processes produce $e^+e^-$ pairs from displaced vertices.
In this thesis, an extension to the track reconstruction is presented, which is required to reconstruct such electrons. The momentum resolution that is achieved with the extension is found to be as good as the standard reconstruction. The acceptance of tracks with low transverse momentum is improved. Applying the extended reconstruction to simulated Standard Model muon decays results in an increase of 80 % in reconstructed conversion electrons from photons of the decay $\mu^+ \to e^+\overline{\nu}_\mu\nu_e\gamma$. Reconstructing $e^+e^-$ vertices from this decay and other processes yields a map of the material distribution within the detector. In addition, the decay of simulated dark photons $\mathrm{A}' \to e^+e^-$ with finite lifetime is studied, showing that the dark photon mass can be reconstructed with an average resolution of $\sigma_m = 0.7\,\mathrm{MeV}/c^2$.
It is shown that the reconstruction of electrons from displaced vertices performs as expected, and thus, new possibilities are opened up for the *Mu3e* detector to investigate further physics processes.

**Spur-Rekonstruktion von Photonkonversionselektronen im *Mu3e*-Detektor**

Die *Mu3e*-Kollaboration sucht nach dem Leptonfamilienzahl-verletzenden Zerfall $\mu^+ \to e^+e^-e^+$ mit einem Detektor basierend auf dünnen Silizium-Pixel-Sensoren. Um Vielfachstreuung zu reduzieren, ist das Materialaufkommen im Detektor minimiert. Dadurch ist er optimal geeignet, Elektronen mit niedrigem Impuls mit hoher Genauigkeit zu rekonstruieren, und kann ebenfalls genutzt werden, um nach Neuer Physik in weiteren seltenen Prozessen im Niedrigenergiebereich zu suchen, oder um Präzisionsmessungen durchzuführen. Viele dieser Prozesse erzeugen $e^+e^-$-Paare von versetzten Vertices.
In dieser Arbeit wird eine Erweiterung der Spur-Rekonstruktion vorgestellt, die nötig ist, um solche Elektronen zu rekonstruieren. Die hiermit erreichte Impulsauflösung ist genauso gut wie die der ursprünglichen Rekonstruktion. Die Akzeptanz von Spuren mit niedrigem Transversalimpuls wird verbessert. Die Anwendung der erweiterten Rekonstruktion auf simulierte Standardmodell-Myonenzerfälle ergibt einen Anstieg von 80 % in der Anzahl rekonstruierter Spuren von Konversionselektronen, die von Photonen aus dem Zerfall $\mu^+ \to e^+\overline{\nu}_\mu\nu_e\gamma$ stammen. Die Rekonstruktion von $e^+e^-$-Vertices aus diesem und anderen Zerfällen ergibt ein Abbild der Materialverteilung im Detektor.
Darüber hinaus wird eine Studie zum Zerfall simulierter dunkler Photonen $\mathrm{A}' \to e^+e^-$ mit endlicher Lebensdauer durchgeführt, die zeigt, dass die Masse des dunklen Photons mit einer durchschnittlichen Auflösung von $\sigma_m = 0.7\,\mathrm{MeV}/c^2$ rekonstruiert werden kann.
Es wird gezeigt, dass die Rekonstruktion von Elektronen von versetzten Vertices wie erwartet funktioniert, und sich damit neue Möglichkeiten eröffnen, mit dem *Mu3e*-Detektor weitere physikalische Prozesse zu untersuchen.

# Contents

# 1. Introduction

Since neutrino oscillation has been observed, the violation of lepton flavor in neutral current weak interactions is a well established extension to the Standard Model of particle physics. This raises increasing interest in studying lepton flavor violation in charged current interactions. The *Mu3e* experiment is dedicated to searching for such a violation in the decay $\mu^+ \to e^+e^-e^+$ with a final sensitivity of 1 in $10^{16}$ decays [Blo+13]. In the extended Standard Model, which accounts for finite neutrino masses, this decay is only possible at loop-level through neutrino mixing and is therefore so highly suppressed as to be beyond experimental reach. Consequently, the observation of a signal would prove that lepton flavor conservation is also violated in charged current interactions and therefore be a clear indication for physics beyond the Standard Model.

A new detector is being developed for the *Mu3e* experiment, based on thin silicon pixel sensors. This technology allows for an extremely low material budget, minimizing multiple Coulomb scattering and permitting high momentum resolution and background suppression in track and vertex reconstruction of low-momentum electrons and positrons.

In order to achieve the desired sensitivity, the detector is designed to deal with an extremely high intensity beam and handle high data rates, and can therefore be applied to several additional searches for rare processes and precision measurements. These include the search for dark photons $\mathrm{A}'$, which would be emitted in the muon decay $\mu^+ \to e^+\overline{\nu}_\mu\nu_e\mathrm{A}'$, and subsequently decay into an electron-positron pair $\mathrm{A}' \to e^+e^-$. The dark photon decay can occur promptly or delayed, for dark photons with a finite lifetime. Especially for long-lived dark photons with displaced decay vertices, *Mu3e* can conduct a search in a previously not excluded mass region.

Besides the *Mu3e* signal decay, there is another lepton flavor violating decay, $\mu^+ \to e^+\gamma$, that can be investigated. With a modified detector to enhance photon conversion, the sensitivity predicted by current experimental plans could be surpassed by one order of magnitude down to a single event sensitivity of $7 \times 10^{-15}$ [Che+13].

At the *Paul Scherrer Institute*, where the *Mu3e* experiment is situated, a high intensity $\pi^-$ beam is also available. Using neutral pions from charge exchange $\pi^-p \to \pi^0n$, this offers the possibility to apply the *Mu3e* detector to measuring the Dalitz decay $\pi^0 \to e^+e^-\gamma$, which can improve the precision of the electromagnetic transition form factor. As the form factor enters into the calculation of the hadronic light-by-light contribution to the theoretical value for the anomalous magnetic moment of the muon $a_\mu$, a higher precision helps to prove or disprove the discrepancy

of currently 3.6 standard deviations between the experimental and the theoretical value for $a_\mu$ [Eid16]. Additionally, the Dalitz decay can be used to search for dark photons, which can appear in the pion decay $\pi^0 \to \mathrm{A}'\gamma$. Here, the dark photon mass would be given by a resonance on the spectrum of the invariant mass of the $e^+e^-$ pair from the Dalitz decay.

Reconstructing photon conversion events is interesting in its own right, as the conversion rate is directly linked to the material density. Thus, reconstructing the vertex position of $e^+e^-$ track pairs provides a map of the material distribution within the detector. This knowledge is crucial for the understanding of the detector geometry.

All of the above mentioned processes produce displaced vertices of $e^+e^-$ pairs either from photon conversion or from the decay of dark photons. Reaching the desired levels of sensitivity requires these events to be reconstructed with high precision, especially as the conversion probability is low due to the low material budget. The standard *Mu3e* track reconstruction, developed to reconstruct signal decay products, requires an electron to produce at least one hit in each of the four pixel layers to be reconstructable. As Standard Model photons and long-lived dark photons can traverse matter without interacting, it is necessary to extend the algorithm to include tracks originating from displaced vertices outside of the first detection layer. The work presented here concentrates on this extension of the existing track reconstruction implementation in three steps:

1. Implementation of the necessary extensions.
2. Analysis and optimization of the performance.
3. Application to different simulated processes.

The studies show that the extension performs as well as the standard *Mu3e* track reconstruction in regard to photon conversion events. It yields an average momentum resolution of $\sigma_p = 0.2\,\mathrm{MeV}/c$ for electrons and positrons with momenta between 10 and $50\,\mathrm{MeV}/c$. The total number of reconstructed tracks from photon conversion events increases by 80 %. The reconstruction of photon conversion events from Standard Model processes gives the expected material map. However, a better background suppression is needed before the material distribution in the final detector can be reliably mapped. A preliminary study of dark photon decays shows that the dark photon mass can be found from the invariant mass of the $e^+e^-$ track pair with an average resolution of $0.7\,\mathrm{MeV}/c^2$.

# 2. Theory

## 2.1. The Standard Model and Beyond

The Standard Model of particle physics is a quantum field theory describing all currently known fundamental particles and their interactions [Tho13], illustrated in figure 2.1. The twelve fermionic spin-$\frac{1}{2}$ matter particles are grouped into three families, holding four particles each that differ from the next family only in mass and lifetime. In addition, there exists an anti-fermion for every fermion with the opposite charge but exactly the same mass.

The particles interact with each other through the exchange of force-carrying gauge bosons with spin-1 corresponding to the quantum field theory describing each force. The forces described by the Standard Model are the strong force, mediated by eight massless gluons g, the electromagnetic force, mediated by the massless photon $\gamma$, and the weak force, mediated by three heavy gauge bosons, the $W^{\pm}$ bosons and the $Z^0$ boson.

The Higgs boson is the only scalar particle in the Standard Model. It is required for the mechanism that generates the mass of the fundamental particles.

The gravitational force is not included in the Standard Model, as it is not described by a quantum field theory. However, between two elementary particles it is very small and can be neglected.

As the twelve fermions interact through different forces, they can be grouped correspondingly: Quarks are sensitive to all forces, charged leptons interact through electroweak forces, and neutral leptons only participate in weak interactions. In the first family, there is the up-quark, the down-quark, the electron and the electron neutrino. These are the constituents of everyday matter. Exotic matter is made up from fermions of the second and third family, which have a successively higher mass and, in the case of charged leptons, decreasing lifetimes. Up-type quarks in higher families are the charm- and the top-quark, while strange- and bottom-quark are down-type quarks. Leptons and their neutrinos are assigned lepton numbers: $L_e$ for the electron, $L_\mu$ for the muon in the second family and $L_\tau$ for the tau in the third family. Lepton number is originally a conserved quantity in the Standard Model, although this has been disproved for the neutral leptons by the observation of flavor-changing neutrino oscillations, for example at the *Super-Kamiokande* experiment [Fuk+98]. To explain these, an extension to the Standard Model is made, where the flavor-state neutrinos are described as a quantum-mechanical

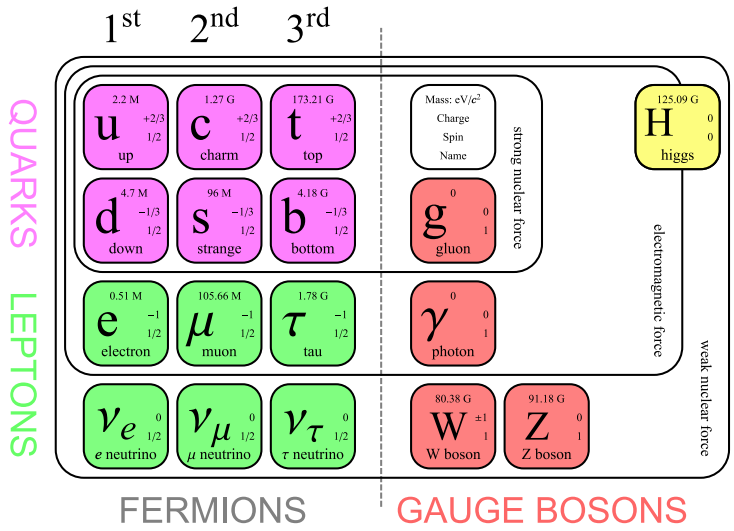


**Figure 2.1.:** The fundamental particles in the Standard Model: three families of fermions, five force-carrying gauge bosons and the Higgs boson, designed by [M L17]. The masses of the particels are given, as well as the electric charge and the spin.

mixture of three fundamental states with finite masses. This extension is by now well-established although the neutrino masses have not yet been determined.

The Standard Model has been tested to high precision and has many times been correct in its predictions, nonetheless it leaves several open questions and unexplained observations. For example, it is not understood why there are exactly three particle families and why the theory observes certain patterns and symmetries. Neither does it account for the values of the 26 free parameters that are determined purely by experiment, nor offer an explanation for the existence of dark matter, for which cosmological and astrophysical experiments provide strong evidence, nor for the matter-antimatter asymmetry in the universe that traces back to the Big Bang.

There are multiple different theories, among others supersymmetric and grand unified models or models with an extended Higgs sector, trying to explain the physics beyond the Standard Model. Different experiments are trying to constrain these models by searching for new phenomena or setting limits on theoretical predictions. One of these is the *Mu3e* experiment.

### 2.1.1. The Muon Decay

The *Mu3e* experiment aims to observe new physics by searching for a transition from the second family muon to the first family electron in order to investigate whether lepton number is also violated in the charged lepton sector.

The muon has a mass of $105.7\,\mathrm{MeV}/c^2$ and a lifetime of $2.2 \times 10^{-6}\,\mathrm{s}$ [Pat+16]. It mainly decays through the Michel decay $\mu^+ \to e^+ \nu_e \overline{\nu}_\mu$ into a positron and two

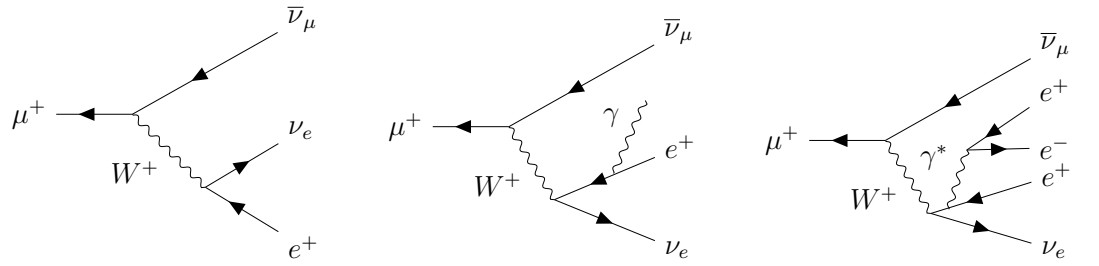


**(a)** The Michel decay is the main decay channel of the muon, with $\mathcal{B} \approx 100\,\%$.

**(b)** The radiative decay of the muon has a branching ratio of $\mathcal{B} = 1.4(4)\,\%$.

**(c)** The internal conversion decay is very rare with a branching ratio of $\mathcal{B} = 3.4(4) \times 10^{-5}$.

**Figure 2.2.:** The Standard Model decays of the muon [Pat+16].

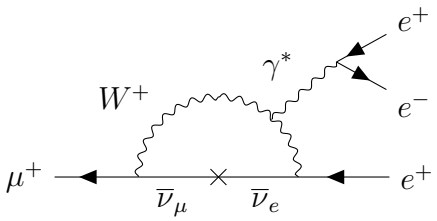


**Figure 2.3.:** Extended Standard Model decay of $\mu^+ \to e^+e^-e^+$ through neutrino mixing at loop level.

neutrinos. Further decays that are allowed in the Standard Model are the radiative decay $\mu^+ \to e^+\gamma\nu_e\overline{\nu}_\mu$ with an additional photon (branching ratio $\mathcal{B} = 1.4(4)\,\%$), and the internal conversion decay $\mu^+ \to e^+e^-e^+\nu_e\overline{\nu}_\mu$, where an off-shell photon decays into an $e^+e^-$ pair ($\mathcal{B} = 3.4(4) \times 10^{-5}$) [Pat+16]. The three Standard Model decays are shown in figure 2.2.

There are multiple theories, for example in [Bu+08; Mih+13], predicting lepton flavor violating decay channels, among others $\mu^+ \to e^+\gamma$, muon conversion on nuclei $\mu^+N \to e^+N$ and $\mu^+ \to e^+e^-e^+$.

The latter can occur in the extended Standard Model at loop level through neutrino mixing, see figure 2.3. But with a branching ratio smaller than $10^{-54}$ this is highly suppressed due to the small ratio of the neutrino mass difference and the W mass $\left(\Delta m_{\nu_{1,2}}/m_W\right)^2$. It is therefore outside the scope of experimental observation. An increased branching ratio is predicted for example by supersymmetric theories (SUSY) [Bar+95] at loop level (figure 2.4a) and can even occur at tree level mediated by new particles like a Higgs-type particle or a new massive vector boson Z′, which is predicted by most of the aforementioned theories [Mur02], and can be seen in figure 2.4b.

The muon can also decay to an electron and a photon through neutrino oscillations at similarly low branching ratios. This can again be strongly enhanced in SUSY

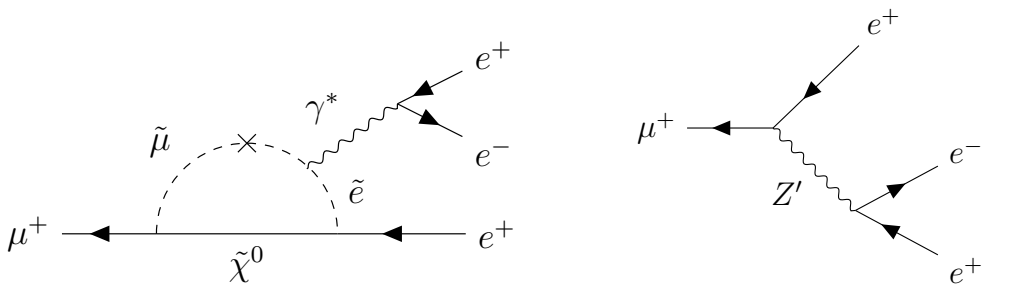


**(a)** $\mu^+ \to e^+e^-e^+$ decay with SUSY sleptons in the loop.

**(b)** Tree level $\mu^+ \to e^+e^-e^+$ decay mediated by a Z′ boson.

**Figure 2.4.:** Lepton flavor violating $\mu^+ \to e^+e^-e^+$ decays.

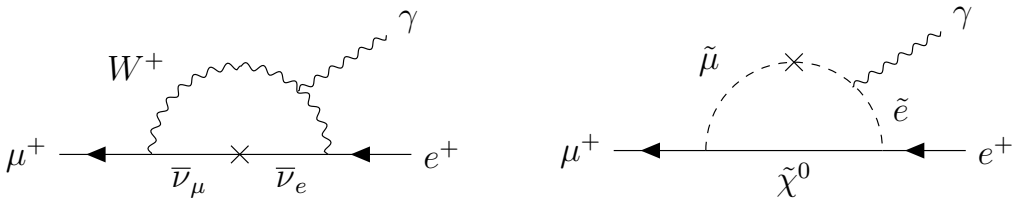


**(a)** Decay of a muon to an electron and a photon through neutrino mixing at loop level.

**(b)** $\mu \to e\gamma$ decay with SUSY particles in the loop.

**Figure 2.5.:** $\mu \to e\gamma$ decays through neutral and charged lepton flavor violation.

theories where it occurs with SUSY particles in a loop [Che+13]. Both cases are shown in figure 2.5.

This decay channel has been investigated by the *MEG* experiment [Bal+16], details of the outcome are summarized in chapter 3.1.

### 2.1.2. The $g-2$ Anomaly of the Muon Magnetic Moment

A strong hint for physics beyond the Standard Model is the discrepancy between the measurement and the theoretical prediction of the magnetic moment of the muon $\vec{\mu} = g_\mu \frac{e}{2m_\mu}\vec{s}$, where $g_\mu$ is the gyromagnetic ratio ($g_\mu = 2$ for Dirac fermions), $e$ is the elementary charge, $m_\mu$ the muon mass and $\vec{s}$ the muon spin. The anomaly $a_\mu = (g_\mu - 2)/2$ is measured and calculated to very high precision and shows a

difference of 3.6 standard deviations between the experimental and theoretical values [Eid16]:

$$a_\mu^{\text{exp}} = 11\,659\,209(6) \times 10^{-10} \tag{2.1}$$

$$a_\mu^{\text{th}} = 11\,659\,180.3(49) \times 10^{-10} \tag{2.2}$$

$$a_\mu^{\text{exp}} - a_\mu^{\text{th}} \quad \hat{=} \quad 3.6\sigma. \tag{2.3}$$

In order to prove or disprove this deviation, the theoretical as well as the experimental value have to be known to greater precision. There are several contributions to the theoretical value from the electromagnetic sector ($a_\mu^{\text{QED}}$), the electroweak sector ($a_\mu^{\text{EW}}$) and the hadronic sector ($a_\mu^{\text{had}}$)

$$a_\mu^{\text{th}} = a_\mu^{\text{QED}} + a_\mu^{\text{EW}} + a_\mu^{\text{had}}. \tag{2.4}$$

The contribution from the hadronic sector is in turn composed of leading order (LO) and higher order (HO) contributions from vacuum polarization and light-by-light (LBL) scattering

$$a_\mu^{\text{had}} = a_\mu^{\text{had, LO}} + a_\mu^{\text{had, HO}} + a_\mu^{\text{had, LBL}}. \tag{2.5}$$

Light-by-light scattering are diagrams of the form shown in 2.6a, where there can be quarks or light mesons in the loop, which can be calculated using lattice QCD and QED [Bij+16]. One factor that enters into the calculation of the hadronic light-by-light scattering is the electromagnetic transition form factor, the value of which is determined experimentally. Operating the *Mu3e* detector with a pion beam, opens up the possibility to measure the Dalitz decay of the neutral pion $\pi^0 \to e^+e^-\gamma$, see figure 2.6b. This could potentially improve the precision of the form factor.

### 2.1.3. Dark Photons

A possible explanation for the $g-2$ anomaly and other discrepancies in the Standard Model involves a new light vector boson that interacts with Standard Model particles by mixing with the electromagnetic $\text{U}(1)_{\text{EM}}$ gauge group. One candidate proposed in several theories [Ess+13] is a dark photon A′. Its coupling strength to charged Standard Model particles is reduced by a factor $\epsilon$, called mixing parameter, compared to the photon coupling. In general, this particle is a good candidate for non-thermal dark matter [Pat+16], but only below the mass range accessible by *Mu3e* [Bau17].

The *Mu3e* experiment can search for dark photons that couple to electrons or muons as illustrated in figure 2.7 if they decay into an $e^+e^-$ pair inside the detector

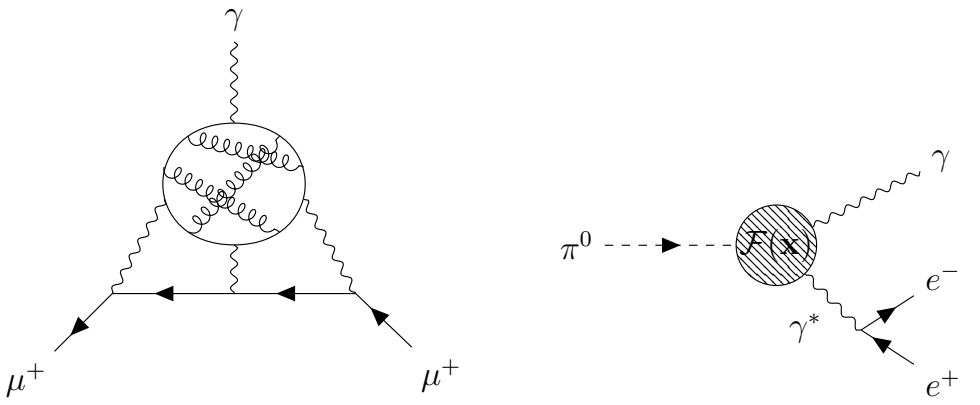


**(a)** Hadronic light-by-light scattering contribution to the magnetic moment of the muon. The main particles in the loop are mesons, especially the neutral pion [Bij+16].

**(b)** The Dalitz decay of the neutral pion with form factor $\mathcal{F}(x)$. $\mathcal{B}(\pi^0 \to e^+e^-\gamma) = 1.17\,\%$ [Pat+16].

**Figure 2.6.:** Contributions to the anomalous magnetic moment of the muon.

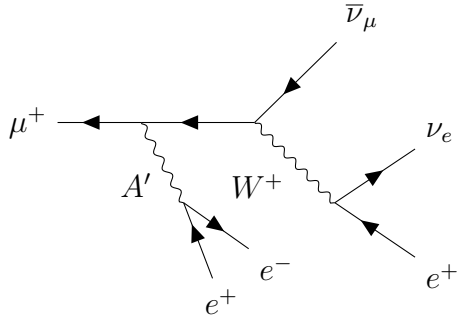


**Figure 2.7.:** An example of dark photon production and decay to $e^+e^-$ in the muon Michel decay. The dark photon can also be radiated off the electron or the $W^+$.

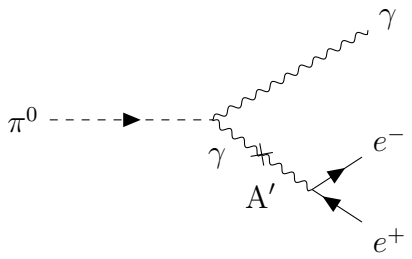


**Figure 2.8.:** Dark photon production in the pion decay $\pi^0 \to \mathrm{A}'\gamma$ with promptly following decay of the dark photon $\mathrm{A}' \to e^+e^-$.

$\mu \to e\nu\nu A'$, followed by $A' \to ee$ as discussed in [Ech+15]. The accessible mass range in muon decays lies within $2m_\mathrm{e} < m_{A'} < m_\mu$.The main characteristic of this decay is the finite invariant mass from a production of an $e^+e^-$ pair and possibly displaced vertices for long-lived dark photons.

As the decay $\mathrm{A}' \to e^+e^-$ is the highly dominant channel in the eligible mass range, the total decay width is given by [Bat+09]

$$\Gamma_{\mathrm{A}'} \approx \frac{1}{3}\alpha\epsilon^3 m_{\mathrm{A}'}\sqrt{1-\frac{4{m_\mathrm{e}}^2}{m_{\mathrm{A}'}^2}}\left(1+\frac{2{m_\mathrm{e}}^2}{m_{\mathrm{A}'}^2}\right), \tag{2.6}$$

with $\alpha$ being the fine-structure constant of electromagnetic coupling, $m_\mathrm{e}$ the electron mass, and $m_{\mathrm{A}'}$ the dark photon mass. Using $c\tau_{\mathrm{A}'} = \hbar c/\Gamma_{\mathrm{A}'}$, the mean life-time of the dark photon is given by

$$c\tau_{\mathrm{A}'} \approx 0.8\,\mu\mathrm{m}\cdot\frac{10^{-6}}{\epsilon^2}\cdot\frac{100\,\mathrm{MeV}/c^2}{m_{\mathrm{A}'}}. \tag{2.7}$$

### Dark Photons in Pion Decays

As mentioned above, the *Mu3e* detector can also be used to analyze neutral pion decays. It is therefore interesting to consider how dark photons can appear in pion decays [Bat15]. Through mixing with the Standard Model photon $\gamma$, a dark photon $\mathrm{A}'$ can be produced in the decay $\pi^0 \to \mathrm{A}'\gamma$, followed by $\mathrm{A}' \to e^+e^-$, see figure 2.8. The expected branching ratio of this decay is

$$\mathcal{B}(\pi^0 \to \mathrm{A}'\gamma) = 2\epsilon^2\left(1-\frac{m_{\mathrm{A}'}^2}{m_{\pi^0}^2}\right)^3\cdot\mathcal{B}(\pi^0\to\gamma\gamma), \tag{2.8}$$

where the mixing parameter $\epsilon$ and the dark photon mass $m_{\mathrm{A}'}$ are the two parameters that characterize the dark photon. The background for this decay is the Dalitz decay of the pion $\pi^0 \to e^+e^-\gamma$. The signature for the dark photon appears as a peak on the spectrum of the invariant mass of the $e^+e^-$ pair.

## 2.2. Particles and Matter

To be able to measure particles with a detector, they need to interact with the detector material. There are many different kinds of interactions, depending on the type of particle, its energy and the detector material. Some of these interactions result in the particle losing kinetic energy. This chapter describes the processes that are relevant for this thesis.

### 2.2.1. Bremsstrahlung and Ionization

Electrons with energies in the range of a few tens of MeV lose energy primarily by Bremsstrahlung when they traverse material. Bremsstrahlung describes the interaction of an electron with the field of a nucleus, whereby the electron loses kinetic energy and a photon is produced, illustrated in figure 2.9a. The energy loss of an electron with initial Energy $E_0$ is given by [GS08]

$$-\frac{\mathrm{d}E}{\mathrm{d}x} \approx 1.37 \times 10^{-7} \cdot \frac{Z^2}{A} \cdot E_0 \ln \frac{183}{Z^{1/3}}, \tag{2.9}$$

where $Z$ and $A$ are the atomic number and the atomic weight of the material and $\mathrm{d}x$ is its thickness. This equation can be written as

$$-\frac{\mathrm{d}E}{\mathrm{d}x} \equiv \frac{E_0}{X_0}, \tag{2.10}$$

defining the the electromagnetic radiation length $X_0$. It is a property of the material the electron traverses and gives the mean distance over which the initial energy is reduced to a factor of $1/e$. That means that an electron with 50 MeV crossing a layer of material with a thickness of $0.1\,\%X_0$ loses approximately 50 keV of its energy.

Towards lower electron energies, the process of ionization plays a role in the total energy loss. It occurs when a free electron interacts with an electron in the shell of an atom and transfers part of its kinetic energy.

For silicon, the critical energy, where energy loss by ionization is equally large as energy loss by Bremsstrahlung, is 39 MeV. The radiation length is 9.4 cm [GS08].

### 2.2.2. Photon Conversion

Uncharged particles, in this case photons, interact differently with material. They can only be detected when they produce charged particles. For photons with energies $E_\gamma > 2\,m_\mathrm{e}\,c^2$, photon conversion, also known as pair production, is the dominant process. It occurs when a photon interacts with the electromagnetic field of a nucleus and converts into an electron-positron pair $\gamma \to e^+e^-$.

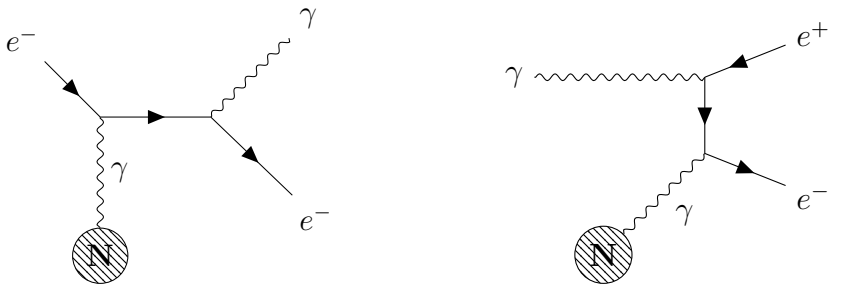


**(a)** Energy loss by an electron interacting with a nucleus N and producing Bremsstrahlung.

**(b)** Photon conversion to an $e^+e^-$ pair in the field of a nucleus N.

**Figure 2.9.:** Interaction of particles and matter.

In this process, shown in figure 2.9b, energy and momentum conservation holds. The kinetic energy of the $e^+e^-$ pair adds up to the total photon energy minus two times the electron mass and the recoil energy of the nucleus

$$E_{\text{kin}}^{e^+e^-} = E_\gamma - 2\,m_\text{e}\,c^2 - E_{\text{recoil}}. \tag{2.11}$$

The energy is distributed between the electron and the positron depending on the photon energy as shown in figure 2.10. The distribution is symmetric and for $E_\gamma$ in the order of 10 MeV it is flat for positrons that carry between 20 % and 80 % of the photon energy. This means that it is for instance just as likely to produce a conversion pair with an energy ratio of 4:1 as it is to produce one with even energy distribution.

The angle between the two daughter particles is such that their total momentum and that of the recoiling nucleus equal the momentum of the photon. For a high energy photon ($E_\gamma \gg 2\,m_\text{e}\,c^2$) and a heavy nucleus this means that the opening angle is close to zero resulting in almost parallel trajectories of the outgoing $e^+e^-$ pair.

In order to give a measure for photon conversion in material, the radiation length is defined as $X_0 = 7/9^{th}$ of the mean free path length. This means that on average only one in 1286 photons crossing a layer of material with a thickness of $0.1\,\%X_0$ converts into an $e^+e^-$ pair [Seg65]. This corresponds roughly to one tracking layer in the *Mu3e* detector, which is detailed in chapter 4.2.

### 2.2.3. Bhabha Scattering

Free positrons can interact with atomic electrons inside a material via Bhabha scattering. This process produces an electron positron pair originating from the same vertex and is therefore background to photon conversion events or dark photon decays. It is illustrated in figure 2.11.

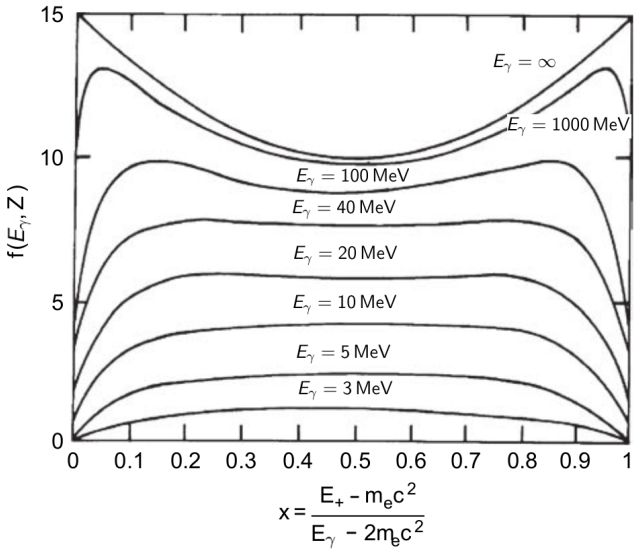


**Figure 2.10.:** The cross section for a positron with fraction $x$ of the total energy to be produced in pair production is proportional to the energy partition function $f(E_\gamma, Z)$ with photon energy $E_\gamma$ and the atomic number $Z$ of the material as parameters, adapted from [GS08].

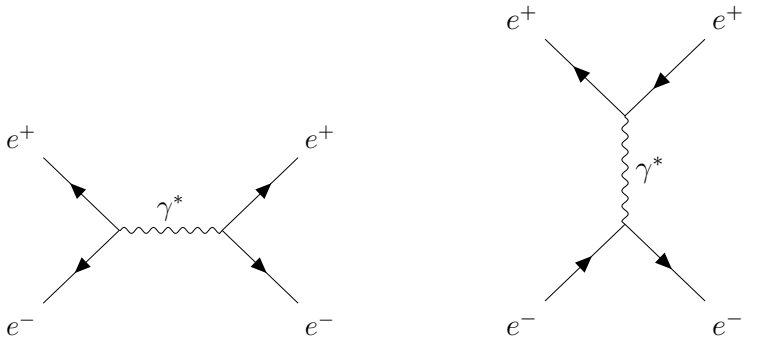


**(a)** $e^+e^-$ pair annihilation and creation.

**(b)** $e^+e^-$ scattering.

**Figure 2.11.:** Bhabha scattering produces an $e^+e^-$ pair originating from the same vertex.

# 3. Current Experimental Status

The latest limit on the branching ratio of the $\mu \to eee$ decay[1] is set by *SINDRUM* in 1988 at $\mathcal{B}(\mu \to eee) < 10^{-12}$ (90 % C.L.) [Bel+88]. The *Mu3e* experiment is designed to continue this search with a single event sensitivity of $1 \times 10^{-16}$ in the final phase. The detector concept, with which to achieve the improvement by four orders of magnitude, is described in chapter 4.2.

As this thesis is motivated by further applications of the *Mu3e* detector, this chapter presents a summary of the current experimental status in the respective areas.

## 3.1. $\mu \to e\gamma$ at *MEG*

The *MEG* experiment at the *Paul Scherrer Institute (PSI)* was searching for the $\mu \to e\gamma$ decay from 2009 until 2013. With a total number of $7.5 \times 10^{14}$ stopped muons and a single event sensitivity of $5.84(21) \times 10^{-14}$ a new limit on the branching ratio was set to $\mathcal{B}(\mu \to e\gamma) < 4.2 \times 10^{-13}$ at 90 % C.L. [Bal+16]. The *MEG* collaboration is planning an upgrade to reach an increased sensitivity of $6 \times 10^{-14}$ [Bal+13] with the *MEGII* experiment.

A proposed upgrade of the *Mu3e* experiment [Che+13] with a photon conversion layer and two additional pixel layers, schematically shown in figure 3.1, could improve this result down to a single event sensitivity of $5 \times 10^{-18}$.

## 3.2. Pion Formfactor

The pion formfactor $\mathcal{F}(x)$ needs to be known to high precision to calculate the hadronic light-by-light contribution to the muon anomalous magnetic moment. The latest measurement of the slope parameter $a$ (from the linear expansion $\mathcal{F}(x) = 1+ax$) is given by the *NA62* experiment as $3.68(57) \times 10^{-2}$ [Cen16]. It was determined from the reconstruction of $1 \times 10^6$ $\pi^0$ Dalitz decays. For *Mu3e* to improve on this result by a factor of two, $4 \times 10^6$ pion Dalitz decays $\pi^0 \to e^+e^-\gamma$ with a branching ratio of $\mathcal{B}(\pi^0 \to e^+e^-\gamma) \approx 1\,\%$ have to be reconstructed. A very rough estimate based on the current design, where the photon conversion rate is in the order of 1 % and the acceptance is approximately 10 %, requires at least $4 \times 10^{12}$ pions to achieve the desired improvement [Ber17].

[1] In the following, muon or $\mu$ stands for $\mu^+$ as the experiment is conducted with positively charged muons and electron or $e$ denotes electrons as well as positrons.

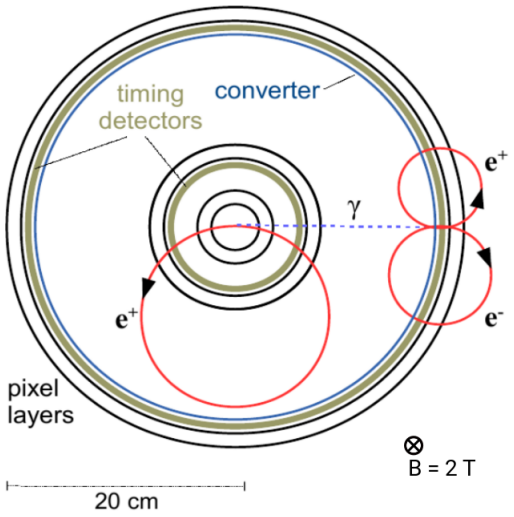


**Figure 3.1.:** Possible upgrade of the *Mu3e* detector with a photon conversion layer, additional pixel and timing layers and an increased magnetic field of $B = 2\,\mathrm{T}$ to measure the decay $\mu \to e\gamma$ with a single event sensitivity down to $5 \times 10^{-18}$ [Sch17].

The high intensity $\pi^-$ beam at the *PSI* provides pions with rates up to $\mathcal{O}(10\,\mathrm{MHz})$ [For97]. Through charge exchange (CEX), $\pi^- p \to \pi^0 n$, neutral pions are produced with a branching ratio of $\mathcal{B}(\mathrm{CEX}) \approx 61\,\%$ [Bas+81]. This rate would result in a run time in the order of several weeks to months to obtain the required number of pions.

## 3.3. Dark Photon Search

Dark photons are searched for in various experiments, therefore the parameter space for the mixing parameter $\epsilon$, describing the coupling strength $\epsilon \cdot e$, versus the mass $m_{A'}$ is already considerably constrained. The projected sensitivity in the search for promptly decaying dark photons for *Mu3e* compared to other experiments is shown in figure 3.2a.

The accessible parameter space can be extended to lower values of $\epsilon$ for dark photons with a finite lifetime. Thus, the *Mu3e* experiment can still contribute to the search, if displaced vertices from $\mathrm{A}' \to e^+e^-$ can be resolved. The colored lines show the square of the mixing parameter $\epsilon^2$ as a function of $m_{\mathrm{A}'}$ for different flight distances at maximal dark photon momentum $p_{\mathrm{A}'}^{\max} = (m_\mu^2 - m_{\mathrm{A}'}^2)/(2m_\mu)$. The space below the lines is covered by dark photons with $p_{\mathrm{A}'} < p_{\mathrm{A}'}^{\max}$. The illustrated mass range between 10 and $100\,\mathrm{MeV}/c^2$ is accessible in muon decays.

### Dark Photons in Pion Decays

The current experimental limits on the mixing parameter $\epsilon$ versus the mass $m_{\mathrm{A}'}$ are shown in figure 3.2b for $m_{\mathrm{A}'}$ between $5\,\mathrm{MeV}/c^2$ and $300\,\mathrm{MeV}/c^2$. Assuming

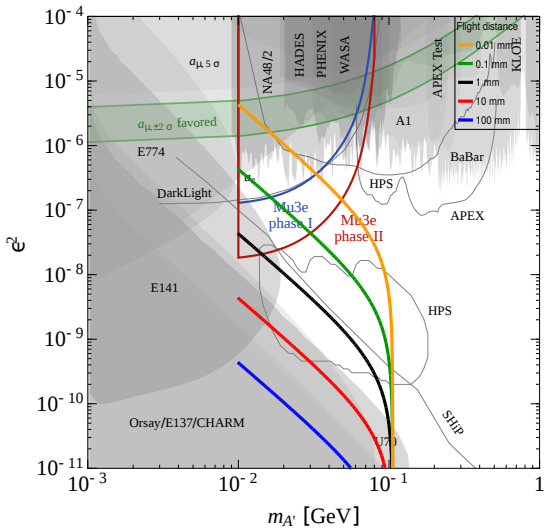


**(a)** Constraints in the search for promptly decaying dark photons from muon decays. Phase I assumes $10^{15}$ stopped muons increasing to $5.5 \times 10^{16}$ in phase II [Ech+15]. The colored lines indicate the extension to lower values of $\epsilon$ for long-lived dark photons with different flight distances. Adapted by [Per14].

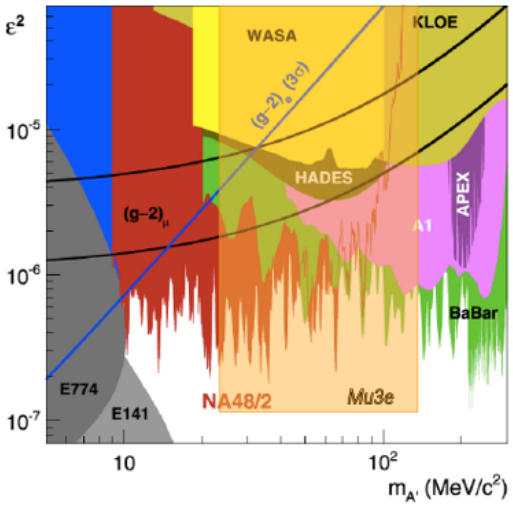


**(b)** Constraints in the search for promptly decaying dark photons in pion decays [Bat15], adapted by [Pap17].

**Figure 3.2.:** Estimates on the constraint the *Mu3e* experiment can put on the parameter space of the mixing parameter $\epsilon$ versus the mass $m_{A'}$ in the search for promptly decaying dark photons.

$\mathcal{O}(10^7)$ reconstructed $\pi^0$ Dalitz decays, *Mu3e* could probe the range of $\epsilon^2$ down to $10^{-7}$ [Pap17], if the background from Dalitz decay and photon conversion can be sufficiently suppressed.

# 4. The *Mu3e* Experiment

In the search for the charged lepton flavor violating decay $\mu^+ \to e^+e^-e^+$ the *Mu3e* experiment faces multiple challenges that are accounted for by a dedicated detector design. In this chapter these challenges and the detector concept are presented as well as the simulation framework for development and preliminary studies. Additionally, the current experimental status and the capacity for improvements that *Mu3e* can achieve for several other measurements are laid out.

## 4.1. Signal and Background

In order to reach the desired sensitivity of one signal decay in $2 \times 10^{15}$ muon decays in phase I ($10^{16}$ in phase II), the experiment utilizes the world's most intense continuous muon beam at the *Paul Scherrer Institute (PSI)* in Switzerland. With very high muon rates of $10^8$ muons/s and an extremely rare signal an excellent background suppression is needed. Therefore, the kinematics of the signal decay and details about the origin of background have to be known and understood to high precision.

### 4.1.1. Signal

The signal decay for the *Mu3e* experiment is a muon decaying into three electrons and nothing else (see figure 4.1).

It is distinguished from the background by applying kinematic arguments. Due to energy and momentum conservation, taking into account that the muon decays

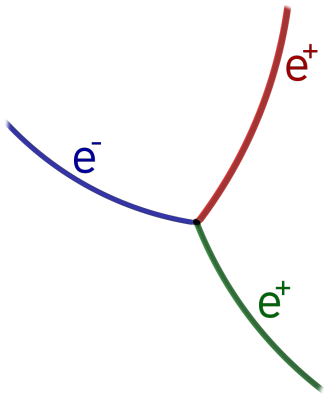


**Figure 4.1.:** Schematic of the signal decay $\mu^+ \to e^+e^-e^+$.

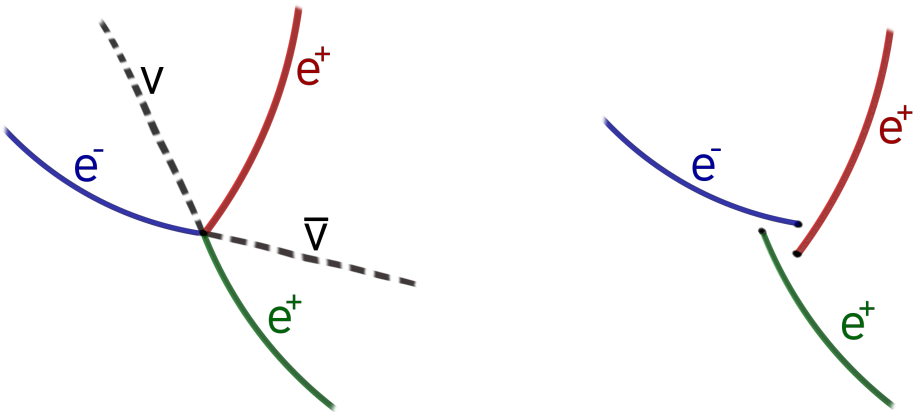


**(a)** Schematics of the internal conversion decay of the muon. Invisible energy is carried away by the neutrinos.

**(b)** Schematics of the combinatorial background. Positrons are mostly supplied by the dominant Michel decay, electrons can originate from Bhabha-scattering or radiative decay and photon conversion. Additional contributions come from mis-reconstructed tracks.

**Figure 4.2.:** Background to the $\mu^+ \to e^+e^-e^+$ decay.

at rest in the laboratory frame, the total momentum of all decay products must equal zero

$$\sum_{i=1}^{3} \vec{p_i} = 0, \tag{4.1}$$

while the maximal momentum one electron can carry corresponds to half the muon mass, approximately 53 MeV/$c$. The total energy must equal the muon mass

$$\sum_{i=1}^{3} E_i = m_\mu c^2. \tag{4.2}$$

All decay products originate from the same vertex and are coincident in time. To be able to identify the signal correctly and distinguish it from background, extremely high vertex, momentum and time resolution are needed.

### 4.1.2. Background

The background to the search for $\mu \to eee$ can be separated into irreducible and accidental background. The former arises from the radiative decay of the muon with internal conversion $\mu \to eee\nu\nu$, schematically shown in figure 4.2a. This decay has a branching ratio of $3.4 \times 10^{-5}$ [Pat+16] and can only be distinguished from the signal decay by identifying the missing energy and momentum carried away by

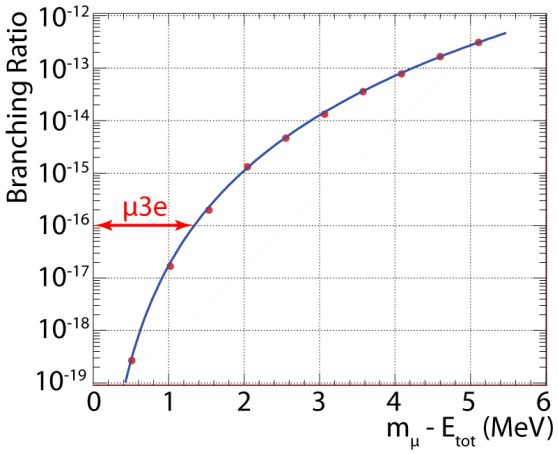


**Figure 4.3.:** Branching ratio for the radiative decay with internal conversion $\mu^+ \to e^+e^-e^+\nu_e\overline{\nu}_\mu$ depending on the neutrino energy $m_\mu - E_{\text{tot}}$ where $E_{\text{tot}}$ is the sum of the energy of the three charged leptons [Dji+09]. *Mu3e* requires this background to be suppressed below a level of $10^{-16}$ and therefore has to provide a momentum resolution better than 1.2 MeV/$c$, or an average of 0.4 MeV/$c$ per electron.

the neutrinos. Figure 4.3 shows the branching ratio of this decay depending on the missing energy $m_\mu - E_{\text{tot}}$. The required level of background suppression to below $10^{-16}$ is included and imposes the energy resolution for all three electrons to be better than 1.2 MeV/$c$. Therefore, the average resolution for one electron has to be at least 0.4 MeV/$c$.

Accidental background arises from combination of particles from different processes, illustrated in figure 4.2b. The dominant source for positrons is the Michel decay $\mu \to e\nu\nu$, which is the main decay channel of the muon. Positrons and electrons can originate from the radiative muon decay with subsequent photon conversion in the target region $\mu \to e\gamma\nu\nu$, $\gamma \to ee$, or with internal conversion if the photon is virtual, and from Bhabha scattering of Michel positrons with electrons in the detector material. Figure 4.4 shows the origin of Bhababa and internal conversion pairs in the inner part of the *Mu3e* detector. The detector structures, which are visible in the vertex distributions, are explained in the following chapter. Additionally, there are contributions from charge mis-identification, if a track is reconstructed in the opposite direction, and mis-reconstruction of tracks. This occurs when non-corresponding hits, produced for example by different particles or noise, are combined. To ensure that no combination of three particle tracks $e^+e^-e^+$ from these events will satisfy the requirements of originating from one vertex at the same time and fulfilling energy and momentum conservation as stated above, excellent vertex position and time resolution are required [Blo+16b].

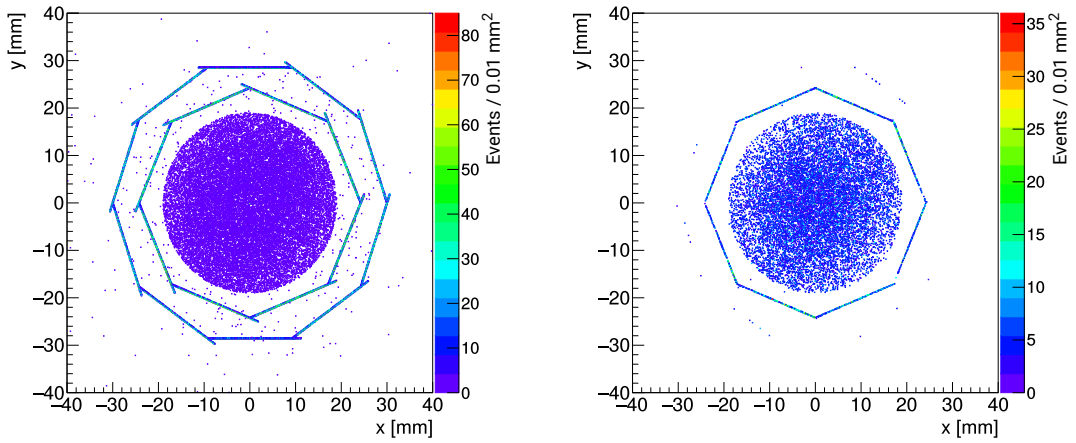


**(a)** Transverse view of Bhabha vertices of $e^+e^-$ pairs in the central part of the detector. Bhabha scattering takes place inside the detector material.

**(b)** Transverse view of the central part of the detector with vertices of $e^+e^-$ pairs from ratiative muon decays with internal conversion. These vertices appear only where muon decays take place.

**Figure 4.4.:** Background electrons in the *Mu3e* detector stem from Bhabha scattering and radiative muon decays with internal conversion.

## 4.2. Detector Concept

In order to reach the desired level of sensitivity and meet the requirements for signal identification and background suppression, the *Mu3e* detector has to be able to stop a large number of muons and measure their decay products with high momentum and vertex resolution. The current design, as used for simulations in this study, is summarized in this chapter [Blo+16b].

As the decay products have a maximum energy of approximately $53\,\mathrm{MeV}/c^2$, corresponding to half the muon mass, the tracking detector has to be designed for low momentum particle reconstruction. In this regime, multiple Coulomb scattering is the dominant source for the uncertainty of the momentum resolution when tracking charged particles traversing the detector material. Compared to this, the spatial uncertainty due to the pixel size is negligible and the momentum resolution $\sigma_p$ for multiple scattering in one layer is proportional to the square root of the material thickness $x$ over radiation length $X_0$ (see equation A.2) [Sch14a; Ber+17]:

$$\frac{\sigma_p}{p} \propto \sqrt{\frac{x}{X_0}}. \tag{4.3}$$

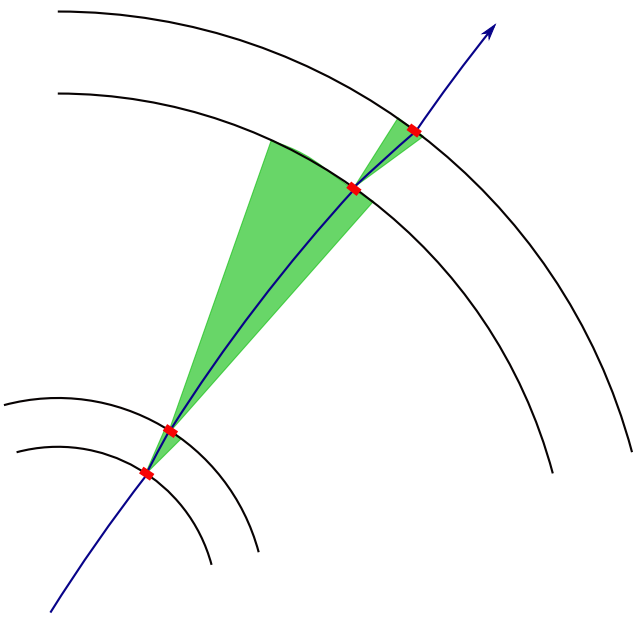

**Figure 4.5.:** Ideal design for tracking in a multiple scattering dominated detector, adapted from [Blo+16b; Sch14a]. This configuration allows the particle a large material free region to bend in the magnetic field, while the material budget can be minimized by reducing the detection layer thickness.

Furthermore, for small scattering angles and short track lengths $s$, $\sigma_p$ can be linearized and is then proportional to the inverse track length $s$:

$$\frac{\sigma_p}{p} \propto \frac{1}{s}. \tag{4.4}$$

In order to optimize the momentum resolution, the material in the active detector volume has to be minimized and the material free region should be maximized for the particle trajectories to propagate without scattering. An ideal configuration is schematically shown in figure 4.5.

### 4.2.1. Pixel Detector

In order to fulfill the requirements discussed above, the *Mu3e* detector is designed as a long axially symmetric cylinder consisting of four layers of silicon pixel sensors and a scintillating fiber detector around a fixed target. The whole detector is placed inside a dry Helium atmosphere that provides gas flow to cool the sensors and reduces multiple scattering compared to air. The muon beam enters the target region through a moderator, slowing down the particles, in between two collimators that ensure a parallel beam. The muons are stopped on a hollow double-cone shaped Mylar target with a length of $l = 10\,\text{cm}$ and radius $r = 19\,\text{mm}$. The cone downstream along the beam direction, has a thickness of $d = 75\,\mu\text{m}$, while the

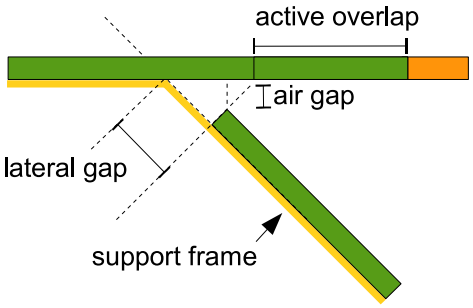


**Figure 4.6.:** Overlap between two ladders with MuPix sensors [Blo+16b].

**Table 4.1.:** Central detector layers: four pixel layers for tracking and one layer of scintillating fibers for timing.

| Layer | Radius | Length | Ladders | Sensors/Ladder | Overlap | Thickness |
|---|---|---|---|---|---|---|
| 1 | 23 mm | 12 cm | 8 | 6 | 2 mm | $4.6‰X_0$ |
| 2 | 30 mm | | 10 | | | |
| 3 | 74 mm | 34 cm | 24 | 17 | 2.5 mm | |
| 4 | 86 mm | 36 cm | 28 | 18 | | |
| fiber | 64 mm | 32 cm | 12 ribbons | 128 fibers/layer | 3 layers | $3‰X_0$ |

upstream cone is thicker with $d = 85\,\mu m$ to ensure a high stopping rate of over 90 %. The target is surrounded by four ultra-thin silicon tracking layers made of High-Voltage Monolithic Active Pixel Sensors (HV-MAPS [Per07]) in a homogeneous solenoidal magnetic field with $B = 1\,T$ field strength. The read-out components are connected directly to the sensor, forming the MuPix chips. They have an active area of $20 \times 20\,mm^2$ containing $256 \times 256$ pixels with a size of $80 \times 80\,\mu m^2$ and are thinned to $50\,\mu m$. The MuPix chips and the electrical layers for read-out, slow control and power supply ($\approx 100\,\mu m$) are glued to a polyimide support structure ($\approx 25\,\mu m$) to form ladders, which the detection layers are comprised of. There is a small overlap of active area between two ladders to increase the acceptance, the layout is illustrated in figure 4.6. One such layer has a thickness of $0.115\,\%X_0$. The layers are connected to aluminum wheels at both ends for mechanical support and service supply, including cabling and cooling. They are spaced in pairs with two shorter vertex layers with a length of $l_{1,2} = 12\,cm$ at $r_1 = 23\,mm$ and $r_2 = 30\,mm$ and two longer outer layers with $l_3 = 34\,cm$ and $l_4 = 36\,cm$ at $r_3 = 74\,mm$ and $r_4 = 86\,mm$, increasing the geometrical acceptance of particles moving up- or downstream. This information is summarized in table 4.1 and the setup is shown in figure 4.7. In the transverse view in figure 4.7b the pixel ladders are visible.

### 4.2.2. Fiber Timing Detector

In addition to the pixel detector, there is a scintillating fiber detector for timing information just inside the third pixel layer at a radius of $r_{\text{fibers}} = 64\,\text{mm}$. It consists of three layers of 128 square fibers each with an edge length of 250 µm.They are arranged in twelve ribbons of length $l = 32\,\text{cm}$. The fibers are coated in 100 nm aluminum and glued together. In total, this corresponds to a thickness of 0.3 % radiation length. The achieved time resolution is approximately 0.4 ns. This information is included in table 4.1 in comparison with the pixel layers. In figure 4.7 the position of the fibers below the third pixel layer can be seen.

This set-up leaves a material free region of $\Delta r = 34\,\text{mm}$ between the second pixel layer and the fiber detector filled only with Helium gas, where the particle trajectory can bend in the magnetic field almost without multiple scattering.

### 4.2.3. Recurl Stations

Up- and downstream of the central detector there are two additional pixel layers, copies of the third and fourth layer of the central detector, for tracking and scintillating tiles for timing. These recurl stations permit a better determination of the momentum of a particle bending in the magnetic field as they allow for a long trajectory inside the Helium atmosphere, avoiding multiple scattering. In addition, multiple scattering effects cancel to first order for trajectories that are allowed to describe a 180° turn, illustrated in figure 4.8. Furthermore, having additional hits per track constrains the reconstruction and reduces the rate of falsely reconstructed tracks.

The scintillating tiles in the recurl stations provide a much higher time resolution than the fibers of approximately 70 ps. As they are placed at the end of a recurling particle's trajectory, their material budget does not have to be minimized. The longitudinal view of the detector in figure 4.7a shows the recurl stations and the instrumentation gap between the central detector and the outer stations.

This detector design optimizes the geometrical acceptance on the one hand and on the other hand it is able to fulfill the resolution requirements by minimizing the material budget. Losses occur for tracks along the beam line with an elevation angle smaller than 20° (see figure A.1) and for tracks with too low transverse momentum, $p_t \lesssim 10\,\text{MeV}/c$, to reach the outermost pixel layer [Blo+16b].

## 4.3. Simulation

In order to optimize the detector geometry, develop the reconstruction software for the *Mu3e* experiment and perform preliminary analytic studies, a simulation of the detector geometry and various physics processes is implemented using the *Geant4* software toolkit [Ago+03]. It provides an elaborate and finely tunable geometric model of the *Mu3e* detector and employs Monte-Carlo methods to simulate the

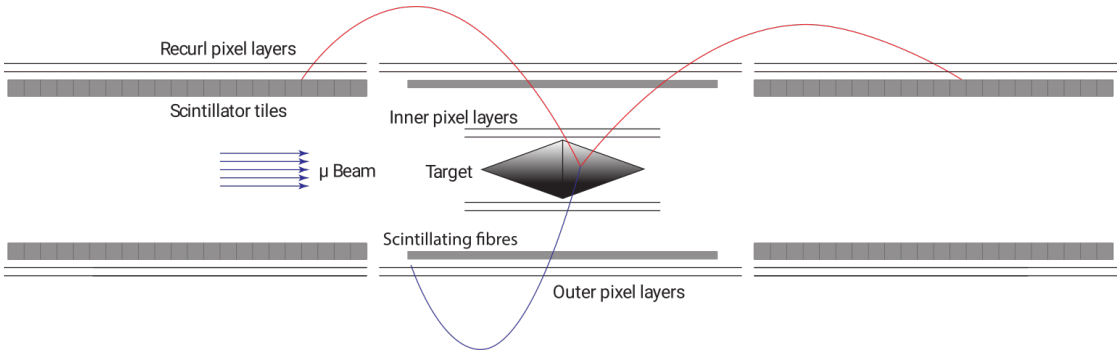


**(a)** Cross section of the *Mu3e* detector along the beam with the central region and the recurl stations on both sides.

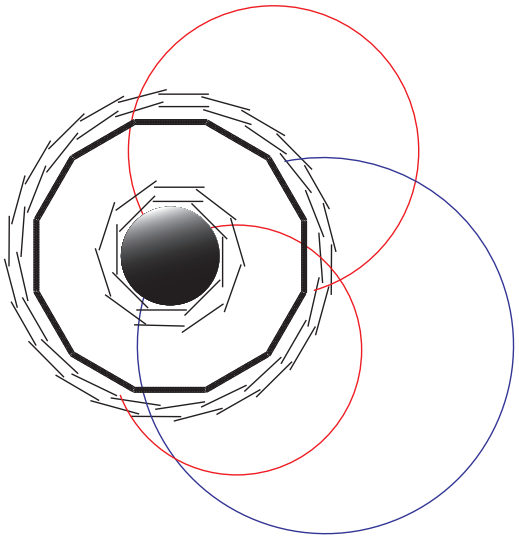

**(b)** Cross section of the *Mu3e* detector orthogonal to the beam line.

**Figure 4.7.:** The *Mu3e* detector with three tracks from a signal decay $\mu^+ \to e^+e^-e^+$ [Blo+16b]. The arrangement of the four pixel layers, consisting of overlapping ladders, around the double cone target can be seen as well as the scintillating timing layers.

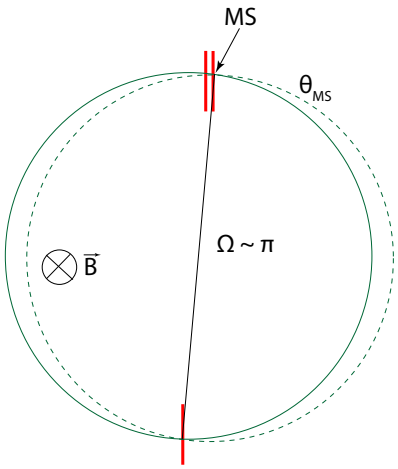


**Figure 4.8.:** Multiple scattering effects cancel approximately after a turn of $\Omega \approx \pi$ of a trajectory in a magnetic field, transverse view [Blo+16b].

interaction of particles with the material, propagate the particle trajectories and register hits in the detection layers [Blo+16b; Sch12]. Several features in the simulation can be changed to execute different Monte-Carlo studies, which can later be compared to measured results. The relevant features and the values used for the studies in this thesis are presented in this chapter.

### 4.3.1. Detector Geometry

The simulation closely adopts the current plans for the detector geometry with all components as described in chapter 4.2. The target suspension is simulated as a nylon wire with diameter $d = 250\,\mu\text{m}$ along the axis and three wires at both ends. The pixel sensors are simulated as $50\,\mu\text{m}$ thick silicon with an active size of $20 \times 20\,\text{mm}^2$ and an inactive area of $0.48 \times 20\,\text{mm}^2$. They are 100 % efficient and noise or charge sharing between pixels is not included in the implementation. The active sensor is located on top of the passive material, which is simplified as an aluminum conductor of $28\,\mu\text{m}$ thickness on $52\,\mu\text{m}$ thick polyimide. The sensor stack is supported by a $25\,\mu\text{m}$ polyimide frame. The fiber layers are simulated with a length of 36 cm, corresponding to the length of the fourth pixel layer.

The coordinate system is right-handed with the origin in the center of the target, the $z$-axis pointing downstream along the magnetic field lines and the $y$-axis pointing upwards. Azimuthal angles, orthogonal to the magnetic field, are denoted by $\varphi$. Elevation angles are either referred to by $\vartheta$ if they are measured from the $z$-axis, or by $\lambda = \frac{\pi}{2} - \vartheta$ if they are measured with respect to the $x - y$ plane. They are illustrated in figure 4.9.

### 4.3.2. Time Frame and Muon Rate

The read-out time frame length for the data acquisition is 50 ns, which is emulated in the simulation.

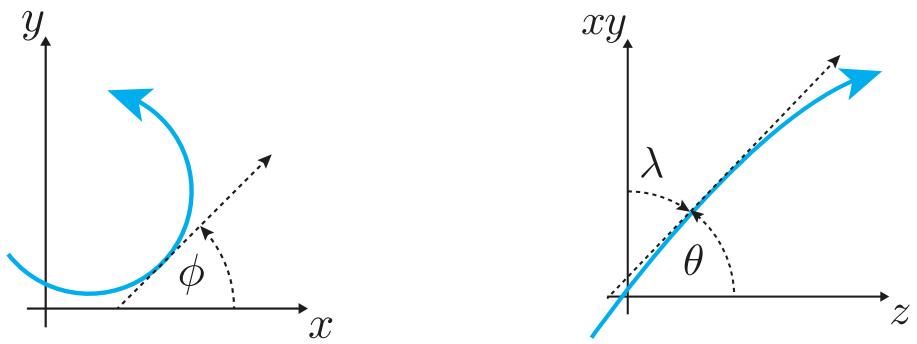


**(a)** Transverse plane with azimuthal angle $\varphi$.

**(b)** Longitudinal plane with elevation angles $\vartheta$ and $\lambda = \frac{\pi}{2} - \vartheta$.

**Figure 4.9.:** Angles in the coordinate system of *Mu3e*. A particel track is shown in blue.

Muons are generated 12 cm upstream of the target center, with an elliptic beam profile. A muon rate of $1.9 \times 10^8$/s results in $10^8$ stopped muons/s on the target. The rest of the muons either decay before the target, do not hit it at all or are not stopped and decay downstream of the target.

### 4.3.3. Physics Processes

As the *Mu3e* detector is based on an ultra-thin silicon pixel tracker and deals with low momentum particles, multiple scattering in the detection material is the main uncertainty for track fitting and the limiting factor for the momentum resolution. The current implementation is based on the multiple scattering distribution provided by *Geant4*, which describes the Gaussian core of the actual scattering distribution well. There is a newly-developed model [Ber+14] that includes a good description of the tail of the distribution. This can be used to improve the simulation of multiple scattering in thin silicon sensors.

In order to study various physics models, multiple decay modes are implemented and can be chosen from for the simulation.

#### Muon Decay

The Standard Model decay modes include the Michel decay of polarized muons as provided by *Geant4* as well as the radiative decay with an updated branching ratio, and the radiative decay with internal conversion. There are more precise calculations available for the description of the Standard Model decays, which will be implemented in the future. The radiative decay is implemented with a minimal photon energy of $E_\gamma = 5\,\text{MeV}$, to avoid the divergence of the branching ratio for small photon energies. The signal decay is simulated as demonstrated by the *SINDRUM* experiment [Bel+88] using phase space distributions for a three body decay.

#### Photon Gun

In order to develop the photon conversion reconstruction a photon gun is implemented. It produces one photon per time frame at the center of the target. The photons are generated with randomized momenta and directions and within an adjustable energy range.

#### Dark Photons

For the study of long-lived dark photon reconstruction, the simulation of the muon decay is extended to radiate a dark photon $\mu \to e\nu\nu\mathrm{A}'$ that decays into an $e^+e^-$ pair. The lifetime and the mass of the dark photon are adjustable.

### 4.3.4. Truth Information

In order to analyze the reconstruction performance, it is necessary to use truth information from the simulation. The relevant variables for the work performed for this thesis are the hit information, including which pixel in which layer was hit, which track caused the hit, if the particle was moving towards the outside or the inside of the detector and how many pixel hits the particle has caused previously. This information is stored by assigning a hit ID and track ID to each hit. If one pixel is hit by two particles within the same time frame, the information for both tracks and their shared hit is available. The track information includes the particle type and its origin, the momentum and the vertex position as well as the direction angles $\varphi$ and $\lambda$ at the first pixel layer.

# 5. Tracking and Vertexing

## 5.1. Multiple Scattering Track Reconstruction

The *Mu3e* experiment deals with particles in the low-energy range with a pixel tracking detector that has very high position resolution. Due to the detector design, only single hit clusters from pixels of the size $80 \times 80\,\mu m^2$ are expected. Therefore, the position resolution is given by the single pixel resolution of $\sigma_{pixel} = 80\,\mu m/\sqrt{12} \approx 23\,\mu m$. This leaves multiple Coulomb scattering as the main uncertainty for track fitting. To account for this, a three-dimensional triplet fit is implemented for the track reconstruction as described in [Ber+17; Sch14b; Sch14a]. The representations in this chapter closely follow the current implementation [Blo+16a].

### 5.1.1. Triplet Parameters

The triplet fit method uses three hits $\mathbf{x_0}, \mathbf{x_1}, \mathbf{x_2}$ from consecutive detection layers and assumes multiple scattering at the middle hit. The resulting triplet with the corresponding angles and distances is illustrated in figure 5.1 in transverse and longitudinal view, where 'transverse' and 'longitudinal' are here and in the following always used with respect to the magnetic field lines. The scattering angles are denoted by $\Phi_{\text{MS}}$ and $\Theta_{\text{MS}}$, the transverse track radii before and after the scattering process are given by $r_1$ and $r_2$ and the respective arc lengths by $s_1$ and $s_2$. The helical trajectories through points $\mathbf{x_0}, \mathbf{x_1}$ and $\mathbf{x_1}, \mathbf{x_2}$, respectively, are described by the bending angles $\phi_i$, with distances $d_i$ and azimuthal angles $\varphi_i$ between points in the transverse plane. In the longitudinal plane, $z_i$ are the distances between points along the field axis and $\vartheta_i$ the elevation angles.

Describing the helical trajectory of a charged particle in a homogeneous magnetic field through three points requires a starting point, an initial direction, the curvature, and the distances to the other two points. Considering multiple scattering theory with the specified material, the scattering angle is needed as an additional parameter to include scattering at the middle hit $\mathbf{x_1}$. In total, the three space points provide enough parameters to describe the triplet.

As small energy losses inside the material due to ionization are corrected for later, one can assume momentum conservation in the first step. The momentum of an electron moving in the magnetic field is directly connected to the three-dimensional helix radius $R$, which is therefore constant for one triplet. For small scattering

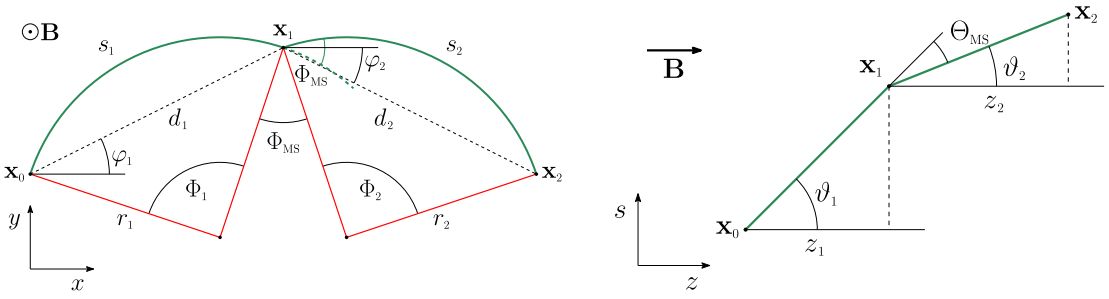


**(a)** Transverse view, projected orthogonal to the beam axis and the magnetic field. The helical trajectories through the three measurement points $\mathbf{x_0}, \mathbf{x_1}, \mathbf{x_2}$ with distances $d_i$ and azimuthal angles $\varphi_i$ between points in the transverse plane are described by the transverse track radii $r_i$, the respective arc lengths $s_i$ and the bending angles $\phi_i$. The scattering angle is denoted by $\Phi_{\mathrm{MS}}$.

**(b)** Longitudinal view, projected onto the plane of the arc length $s$ along the field axis. $z_i$ denote the distances between points and $\vartheta_i$ the elevation angles. The scattering angle in this plane is $\Theta_{\mathrm{MS}}$.

**Figure 5.1.:** Triplet of hits $\mathbf{x_0}, \mathbf{x_1}, \mathbf{x_2}$ with scattering at the middle hit.

angles, the central part of the scattering distribution can be described by the Highland formula, a Gaussian distribution around zero with width [Pat+16; Hig75]

$$\sigma_{\mathrm{MS}} = \frac{13.6\,\mathrm{MeV}}{p\beta c} z \sqrt{\frac{x}{X_0}} \left(1 + 0.038 \log\left(\frac{x}{X_0}\right)\right), \tag{5.1}$$

depending on the radiation length $X_0$ and the material thickness $x$. $\beta c$ is the particle's velocity and $z$ its charge number. The lower the momenta $p$ are, the larger the scattering effects are. In terms of the transverse and longitudinal scattering angles $\Phi_{\mathrm{MS}}$ and $\Theta_{\mathrm{MS}}$ the distribution describes a mean of zero and variances given by $\sigma^2_\Theta = \sigma^2_{\mathrm{MS}}$ and $\sigma^2_\Phi = \sigma^2_{\mathrm{MS}} / \sin^2\vartheta$, the latter reflecting the projection onto the transverse plane.

The $\chi^2$ function that is chosen to describe this problem and has to be minimized is given by

$$\chi^2(R) = \frac{\Phi^2_{\mathrm{MS}}(R)}{\sigma^2_\Phi} + \frac{\Theta^2_{\mathrm{MS}}(R)}{\sigma^2_\Theta}. \tag{5.2}$$

Assuming small scattering angles, which is justified for weak multiple scattering effects, the dependence of the scattering uncertainty $\sigma_{\mathrm{MS}}$ on the particle momentum $p$ can be neglected. Thus, with $\dfrac{\mathrm{d}\sigma_{\mathrm{MS}}}{\mathrm{d}R} = 0$ the equation

$$\Phi_{\mathrm{MS}}(R) \sin^2\vartheta \frac{\mathrm{d}\Phi_{\mathrm{MS}}(R)}{\mathrm{d}R} + \Theta_{\mathrm{MS}}(R) \frac{\mathrm{d}\Theta_{\mathrm{MS}}(R)}{\mathrm{d}R} = 0 \tag{5.3}$$

has to be solved to find the radius $R$ that minimizes the scattering angles for a triplet. The solution does not depend on the scattering uncertainty anymore, so uncertainties for the track parameters can be calculated and easily propagated after fitting.

### 5.1.2. Linearization around the Circle Solution

In the following, geometrical relations between triplet parameters, scattering angles and the radius $R$ are used to solve the problem. The independent scattering angles are given by

$$\Phi_{\mathrm{MS}}(R) = (\varphi_{12} - \varphi_{01}) - \frac{1}{2}\left(\phi_1(R) + \phi_2(R)\right), \tag{5.4}$$

$$\Theta_{\mathrm{MS}}(R) = \vartheta_2(R) - \vartheta_1(R). \tag{5.5}$$

The bending angles $\phi_i$ and $\vartheta_i$ are determined by linearizing the problem and neglecting higher order terms

$$\phi_i = \phi_i^{(0)} + \alpha_i \cdot (R - R_i^{(0)}), \tag{5.6}$$

$$\vartheta_i = \vartheta_i^{(0)} + \beta_i \cdot (R - R_i^{(0)}), \tag{5.7}$$

where $\phi_i^{(0)}$, $\vartheta_i^{(0)}$ and $R_i^{(0)}$ are the values of the initial solution, where the transverse radii are equal ($r_1 = r_2$) and $\Phi_{\mathrm{MS}} = 0$. The derivation $\alpha_i = \mathrm{d}\phi_i/\mathrm{d}R \,|_{\phi_i^{(0)}}$ can be obtained from the helix equations as well as $\beta_i = \mathrm{d}\vartheta_i/\mathrm{d}R \,|_{\vartheta_i^{(0)}}$:

$$r_i \cdot \sin\frac{\phi_i}{2} = \frac{d_i}{2} \qquad \text{(transverse)}, \tag{5.8}$$

$$R^2 \cos^2\vartheta_i \cdot \phi_i^2 = z_i^2 \qquad \text{(longitudinal)}, \tag{5.9}$$

$$\Rightarrow \alpha_i = -\frac{\phi_i^{(0)}}{R_i^{(0)}} \cdot \left(\cos^2\vartheta_i + \frac{\phi_i^{(0)}}{2}\cot\frac{\phi_i^{(0)}}{2}\sin^2\vartheta_i\right)^{-1}, \tag{5.10}$$

$$\Rightarrow \beta_i = -\frac{\cot\vartheta_i}{R_i^{(0)}} \cdot \left(1 + \alpha_i \cdot \left(\frac{\phi_i^{(0)}}{R_i^{(0)}}\right)^{-1}\right). \tag{5.11}$$

The initial solution is a circle in the transverse plane and exists for any hit triplet. Furthermore, as scattering angles are assumed to be small, it is expected to be close to the final solution of the triplet fit. The values can easily be obtained from geometrical considerations by regarding a purely transverse circle through

three points in space, with $d_{02}$ being the distance between the first and the third measuring point $\mathbf{x_0}$ and $\mathbf{x_2}$:

$$\text{transverse radius:} \quad r^{(0)} = \frac{d_{02}}{2\sin(\varphi_{12} - \varphi_{01})}, \tag{5.12}$$

$$\text{radial angles:} \quad \phi_i^{(0)} = 2\arcsin\left(\frac{d_i}{2r^{(0)}}\right), \tag{5.13}$$

$$\text{elevation angles:} \quad \vartheta_i^{(0)} = \arctan\left(\frac{\phi_i^{(0)} r^{(0)}}{z_i}\right), \tag{5.14}$$

$$\text{3-D radii:} \quad R_i^{(0)} = \sqrt{\left(r^{(0)}\right)^2 + \frac{z_i^2}{\left(\phi_i^{(0)}\right)^2}}. \tag{5.15}$$

The initial circle result is improved by performing an iteration step, where the updated values are calculated first for $\phi_i$ with equation 5.6 and $R = r^{(0)}$, and subsequently for $r$ and $\vartheta$ with equations 5.13 and 5.14.

### 5.1.3. Energy Loss Correction

At this point, the energy loss, which occurs whenever the particle traverses a detection layer, can be included. Figure 5.2 shows the simulated energy loss $\delta E$ of all particles in the second pixel layer. The dominant process is Bremstrahlung and for thin material layers the shape is represented by a Landau distribution with long tails towards high losses. It depends on the material distribution in the layer and the path length of the particle inside the material:

$$\delta E = \sum_m \frac{\mathrm{d}E_m}{\mathrm{d}X_0} \cdot X_{0,m}, \tag{5.16}$$

where $\frac{\mathrm{d}E_m}{\mathrm{d}X_0}$ is the energy loss per radiation length for material $m$ and $X_{0,m}$ is the radiation length for the particle's path length, respectively.

The most probable energy loss at the scattering layer is given by

$$\delta R = f_E \cdot \frac{\delta E}{0.3 \cdot B}. \tag{5.17}$$

$f_E = 0.75$ [Pat+16] corrects for the position of the energy loss maximum with respect to the long tail towards higher energy losses and $B$ is the magnetic field.

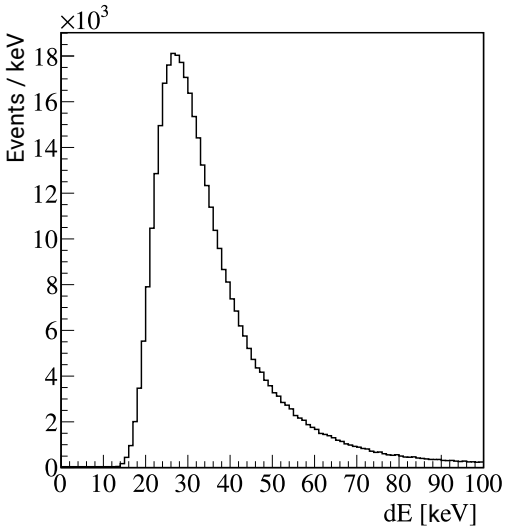


**Figure 5.2.:** Energy loss of all electrons in the second layer. The dominant process is Bremsstrahlung.

The energy loss is included in the track reconstruction by replacing the radius $R$ with $R - \delta R$ in the second helix of a triplet. It can be added up at each layer for succeeding triplets.

### 5.1.4. Final Triplet Parameters

Equations 5.6, 5.7 and the constant energy loss correction $\delta R$ are used to express the scattering angles from equation 5.4 in their linearized form as

$$\begin{aligned}\Phi_{\mathrm{MS}}(R) &= (\varphi_{12} - \varphi_{01}) - \frac{1}{2}\left(\alpha_1 R_1^{(0)} + \alpha_2 R_2^{(0)}\right) - \frac{1}{2}\left(\alpha_1(R - \delta R_1) + \alpha_2(R - \delta R_2)\right) \\ &:= \Phi_{\mathrm{MS}}^{(0)} + \alpha \cdot R, \end{aligned} \tag{5.18}$$

$$\begin{aligned}\Theta_{\mathrm{MS}}(R) &= \vartheta_2^{(0)} - \vartheta_1^{(0)} - \left(\beta_2 \cdot R_2^{(0)} - \beta_1 \cdot R_1^{(0)}\right) + \beta_2(R - \delta R_2) - \beta_1(R - \delta R_1) \\ &:= \Theta_{\mathrm{MS}}^{(0)} + \beta \cdot R. \end{aligned} \tag{5.19}$$

Inserting the derived expressions for the scattering angles into the linearization of the $\chi^2$ function 5.2 simplifies it to

$$\chi^2(R) = \chi^2_{\mathrm{min}} + \frac{(R - R_{\mathrm{min}})^2}{\sigma_R^2}, \tag{5.20}$$

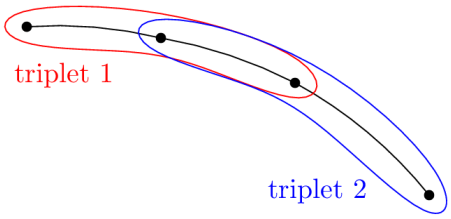


**Figure 5.3.:** In order to fit a track, consecutive triplets are combined so that they share two hits.

where $R_{\text{min}}$ is the three-dimensional radius that solves equation 5.3, $\sigma_R$ is an uncertainty estimate on $R_{\text{min}}$, and $\chi^2_{\text{min}} = \chi^2(R_{\text{min}})$.

$$R_{\text{min}} = -\frac{\sigma_R^2}{\sigma_{\text{MS}}^2}\left(\Phi_{\text{MS}}^{(0)} \cdot \alpha \sin^2\vartheta + \beta \cdot \Theta_{\text{MS}}^{(0)}\right), \tag{5.21}$$

$$\sigma_R^2 := \frac{\sigma_{\text{MS}}^2}{\alpha^2 \sin^2\vartheta + \beta^2}, \tag{5.22}$$

with $\vartheta = \frac{\vartheta_1^{(0)} + \vartheta_2^{(0)}}{2}$ the elevation angle at the scattering layer. The scattering angles can now be found from equations 5.18 and 5.19 using $R_{\text{min}}$ as

$$\Phi_{\text{MS}} = \beta \cdot \frac{\beta\Phi_{\text{MS}}^{(0)} - \alpha\Theta_{\text{MS}}^{(0)}}{\alpha^2 \sin^2\vartheta + \beta^2} \quad \text{and} \tag{5.23}$$

$$\Theta_{\text{MS}} = -\alpha \sin^2\vartheta \cdot \frac{\beta\Phi_{\text{MS}}^{(0)} - \alpha\Theta_{\text{MS}}^{(0)}}{\alpha^2 \sin^2\vartheta + \beta^2} \tag{5.24}$$

### 5.1.5. Fitting Tracks from Triplets

To fit tracks with more than three hits, multiple triplets are combined so that consecutive triplets share two hits as illustrated in figure 5.3. The total $\chi^2$ function is defined as the sum of all individual triplets $i = 1, ..., n$:

$$\chi^2_{\text{total}} = \sum_i^n \chi_i^2, \tag{5.25}$$

as the scattering in one layer is independent from scattering in the other layers. It can therefore be easily updated when additional triplets are added to the track.

Minimizing this global function with the linearized form of the scattering angles is equivalent to a weighted average of the solutions for all triplets:

$$\overline{R}_{\text{min}} = \sum_i \frac{R_{\text{min},i}}{\sigma^2_{R,i}} \tag{5.26}$$

$$\frac{1}{\overline{\sigma}^2_R} = \sum_i \frac{1}{\sigma^2_{R,i}}. \tag{5.27}$$

This weighted mean of all three-dimensional triplet radii is used to calculate the final parameters for each triplet:

$$\phi'_i = \phi_i + \alpha_i \cdot (\overline{R}_{\text{min}} - R_i), \tag{5.28}$$

$$\vartheta'_1 = \vartheta_i + \beta_i \cdot (\overline{R}_{\text{min}} - R_i). \tag{5.29}$$

## 5.2. Conversion Vertex Fit

After the particle tracks have been reconstructed, and if two tracks with the opposite charge are present, the track parameters are used to perform a vertex fit in order to determine their point of origin. For the *Mu3e* framework a linearized approach is applied, assuming multiple scattering at the innermost tracking layer as the only uncertainty. This chapter summarizes the procedure described in [Sch13; KS16; Sch12], which is adapted to reconstruct photon conversion events by [Ger17].

In order to find the common point of origin of two low-momentum tracks bending in the magnetic field, they are propagated backwards into the vertex region. Taking into account multiple scattering at the inner layer, an iterative fit is performed after finding a suitable set of starting values from an initial guess on the vertex position. As the uncertainty stems from multiple scattering, the Highland formula, see equation 5.1, introduced in the previous chapter for the triplet fit, is valid here as well. Likewise, a similar $\chi^2$ function, summed over both tracks, has to be minimized to fit the vertex position $\mathbf{x}_v$:

$$\chi^2(\mathbf{x}_v) = \sum_i^2 \frac{\Phi^2_{\text{MS},i}(\mathbf{x}_v)}{\sigma^2_{\Phi,i}} + \frac{\Theta^2_{\text{MS},i}(\mathbf{x}_v)}{\sigma^2_{\Theta,i}}. \tag{5.30}$$

The transverse and longitudinal scattering angles $\Phi_{\text{MS}}$ and $\Theta_{\text{MS}}$ are parametrised using the hit position in the first layer $\mathbf{x}_H$, and the track angles after scattering $\varphi_1$ and $\theta_1$. The angles are schematically shown in figure 5.4.

The initial vertex position $\mathbf{x}_{v,0}$, used as starting point for the linearized fit

$$\mathbf{x}_v = \mathbf{x}_{v,0} + \Delta\mathbf{x}_v, \tag{5.31}$$

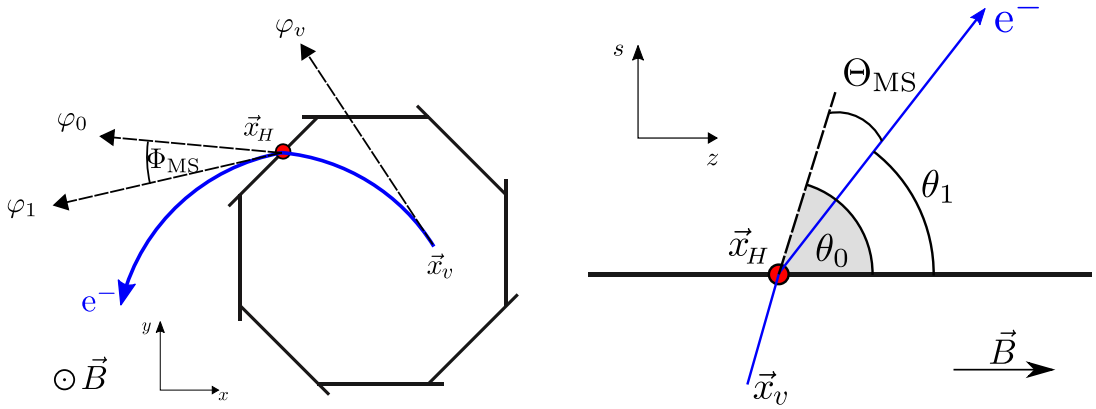


**(a)** Transverse view of the innermost pixel layer. $\varphi_v$, $\varphi_0$ and $\varphi_1$ are the azimuthal track angles at the vertex, before and after scattering at the layer, respectively. The scattering angle $\Phi_{\mathrm{MS}}$ is given by $\Phi_{\mathrm{MS}} = \varphi_1 - \varphi_0$.

**(b)** Longitudinal view. The elevation angle is invariant for a particle moving in the magnetic field **B**. Therefore, the elevation track angle at the vertex is the same as at the hit position before scattering $\theta_0$. After scattering it changes to $\theta_1$. The scattering angle $\Theta_{\mathrm{MS}}$ is given by $\Theta_{\mathrm{MS}} = \theta_1 - \theta_0$.

**Figure 5.4.:** Illustration of scattering at the first pixel layer. The particle track is shown in blue with a hit $\mathbf{x}_H$ in the layer and the vertex at $\mathbf{x}_v$, [Ger17].

is found by considering the transverse projection of the tracks, which is circular. If the two circles intersect, there are two points of intersection. The point with smaller distance in $z$ direction between the tracks is chosen as the starting position in $x$ and $y$, while the mean of the $z$ coordinates gives the initial $z$ position. If the circles do not intersect, the points of closest approach are calculated and mean values of their $x$, $y$ and $z$ coordinates give the starting values.

The other two cases of two circles touching in one point or being identical are so rare as to be numerically impossible and are therefore not considered separately. In practice, they are treated as limits of the first or the second case respectively.

The linearized scattering angles

$$\Phi_{\mathrm{MS},i}(\mathbf{x}_v) = \Phi_{\mathrm{MS},i}(\mathbf{x}_{v,0}) + \Delta\mathbf{x}_v \cdot \nabla\Phi_{\mathrm{MS},i}(\mathbf{x}_{v,0}) \quad \text{and} \tag{5.32}$$

$$\Theta_{\mathrm{MS},i}(\mathbf{x}_v) = \Theta_{\mathrm{MS},i}(\mathbf{x}_{v,0}) + \Delta\mathbf{x}_v \cdot \nabla\Theta_{\mathrm{MS},i}(\mathbf{x}_{v,0}) \tag{5.33}$$

are chosen such that the tracks intersect with the initial vertex position. This is then used to minimize $\chi^2(\mathbf{x}_{v,0} + \Delta\mathbf{x}_v)$ with respect to $\Delta\mathbf{x}_v$. Here, a regularization scale forbids corrections of $\Delta x_v > 1\,\mathrm{mm}$ to prevent overestimation.

After a value for the correction $\Delta\mathbf{x}_v$ has been obtained, the iteration step is performed with the updated vertex position. This is repeated with

$$\mathbf{x}_{v,n+1} = \mathbf{x}_{v,n} + \Delta\mathbf{x}_v. \tag{5.34}$$

The current implementation aims for $\Delta\mathbf{x}_v < 1\,\mu\text{m}$ with up to 1000 iterations.

# 6. Track Reconstruction

The track reconstruction for the *Mu3e* experiment is based on the multiple scattering triplet fit, outlined in chapter 5. The following chapter summarizes the most relevant points of the track reconstruction algorithm as outlined in chapter 28 of [Blo+16a]. The algorithm uses information about the position and timing of the pixel, fiber and tile hits for each time frame. All the steps described in the following take place within one frame of 50 ns.

## 6.1. Fitting Short 4-Hit Tracks

Starting by selecting a hit from the innermost pixel layer and adding one hit from the second and third layers each, the first triplet is formed. Triplets with a transverse radius between 30 mm and 250 mm, being within the geometrical acceptance of the detector, are then initialized, that is to say, the helix parameters are used to calculate the trajectory parameters for the trajectories through the first and second hit and the second and third hit, respectively. From these, the initial values of the scattering angles $\Phi_{\text{MS}}^{(0)}$ and $\Theta_{\text{MS}}^{(0)}$ and of $\chi^2_{\text{min}}$ are derived (see equations 5.18, 5.19 and 5.20). The update step includes the energy loss correction and updates all helix parameters, the scattering angles and the $\chi^2$ value. After the triplet is fitted, it has to fulfill certain criteria before continuing. The track angle is checked at each layer to ensure that the trajectory is outgoing, and the trajectory radius has to be large enough to reach the fourth and outermost pixel layer. A very loose cut on the $\chi^2$ value for the first triplet[1] is applied at $\chi^2 = 100$, reducing the number of falsely reconstructed triplets by a factor of 3 while losing only 0.3 % of correct reconstructions.

In the next step, a hit from the fourth layer is added to the track and the procedure is repeated for both triplets, which are combined considering weights according to equation 5.26. The resulting radius is used to calculate the track parameters. After checking again that the trajectory is outgoing at all hits, and rejecting tracks with $\chi^2 > 32$, the 4-hit track is saved. Exemplary, the reconstructed 4-hit tracks for one frame are shown in figure 6.1a. $\chi^2$-cut efficiencies are shown and explained in chapters 7.1.1 and 7.3. Figure 6.1b shows the $\chi^2$ distribution of 4-hit tracks.

As there exist areas of overlap at the edges of the pixel ladders, an electron can cause two hits in one layer, illustrated in figure 6.2. Two tracks that differ only

[1] Note that the there is only one degree of freedom for a triplet, therefore the $\chi^2$ distribution peaks at zero.

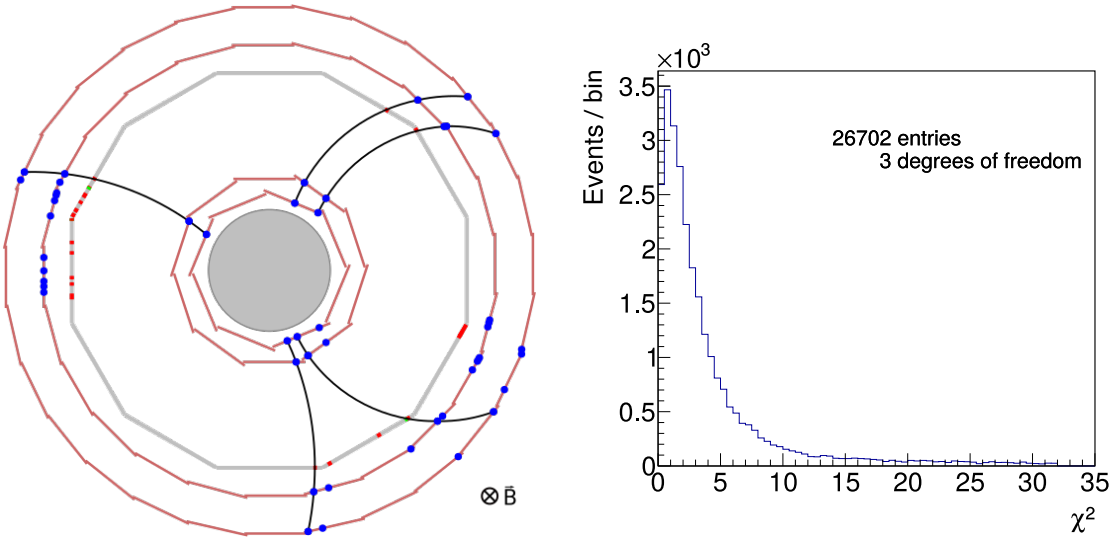


**(a)** Transverse view of the detector with pixel hits (blue), fiber hits (red) and tile hits (green). Five correctly fitted 4-hit tracks are shown. The illustrated event is produced by a photon converting to an $e^+e^-$ pair in the target region.

**(b)** $\chi^2$ distribution of reconstructed 4-hit tracks, which have three degrees of freedom. The cut at $\chi^2 = 32$ gives more than 99 % efficiency at a purity of 89 %.

**Figure 6.1.:** Reconstruction of short 4-hit tracks. Here, for electrons from converted photons from a photon gun.

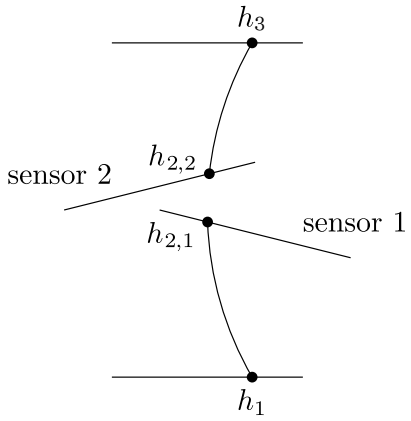


**Figure 6.2.:** A doublet of hits $h_{2,1}$, $h_{2,2}$ in the second layer due to overlapping sensors. The first helix of the triplet is defined by hits $h_1$, $h_{2,1}$ and the second by hits $h_{2,2}$, $h_3$.

in one layer, where they hit adjacent pixel sensors, are therefore merged into one track with a double hit. A 4-hit track can consist of up to four double hits, adding up to effectively eight hits.

## 6.2. Long 6- and 8-Hit Tracks

The reconstruction procedure produces three different types of tracks. The first type, described above, is the short 4-hit track with one hit from every pixel layer in the central detector. These tracks are reconstructed online and are used for event selection and data reduction, by saving only frames with two positively and one negatively charged track from a common vertex.

In the offline reconstruction, the additional hits of recurling particles are considered as well. If the particle bending in the magnetic field hits the central detector or the recurl stations after it has first left the detector, at least two additional hits are produced in the two outer layers. This situation is shown in figures 6.3 and 6.4. Two additional hits are added to a 4-hit track in the same way as described above to form triplets and combine them to tracks, whereupon tracks with $\chi^2 > 48$ are rejected. This method produces long 6-hit tracks with a greatly improved momentum resolution due to the large bending of $\Omega \approx \pi$ in the magnetic field, as explained in chapter 4.2.

If the particle recurls into the central part of the detector and hits the vertex layers again, long 8-hit tracks can be reconstructed by combining two 4-hit tracks. In both cases, the fit is performed to yield updated global track parameters. The resulting $\chi^2$ distributions of the track fit are shown in the appendix A.4.

The *Mu3e* detector is particularly designed for measuring long 6- and 8-hit tracks, as only these yield the excellent momentum resolution required in the experiment. This can bee seen exemplary in figure 6.5, which shows the momentum resolution of 6-hit tracks for different particle momenta.

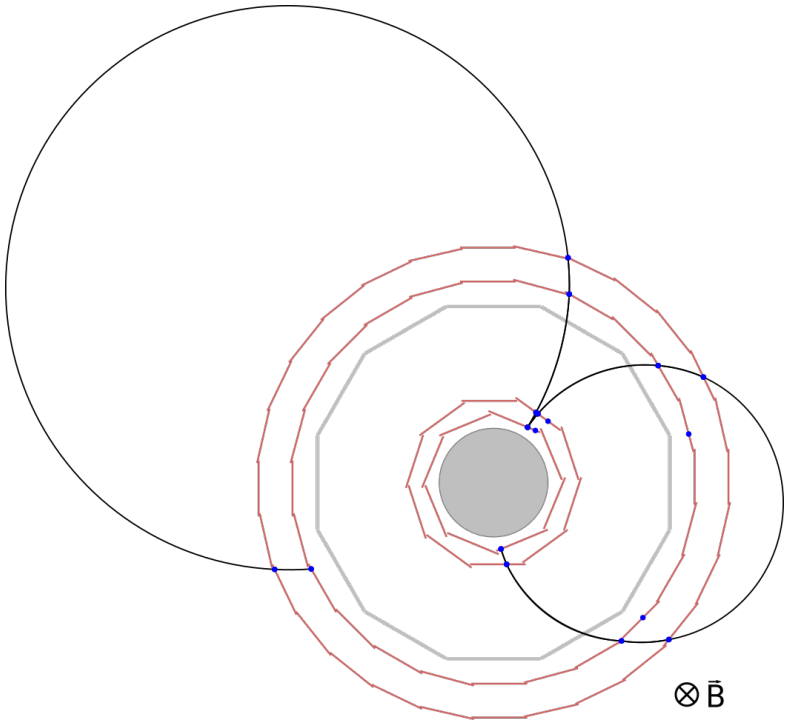


**Figure 6.3.:** Transverse view of the detector with pixel hits (blue). A 6-hit track from a positron and an 8-hit track from an electron recurling into the vertex layers of the central detector are shown.

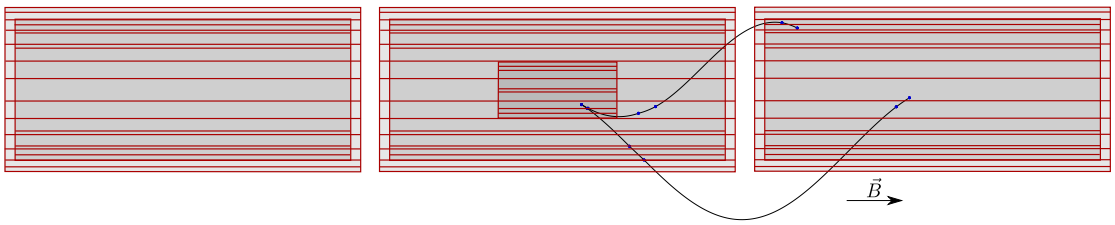


**Figure 6.4.:** Longitudinal view of the pixels (red) in the detector and the recurl stations. Two 6-hit tracks from an electron-positron pair recurling into the recurl stations are shown.

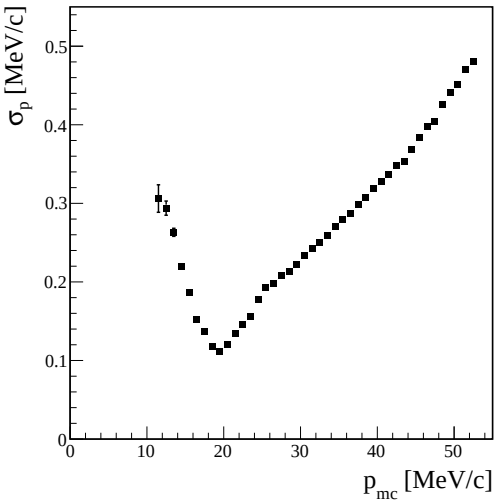


**Figure 6.5.:** Momentum resolution $\sigma_p$ of long 6-hit tracks as a function of the simulated particle momentum $p_{\mathrm{mc}}$.

## 6.3. Timing Information

If an electron is produced with high transverse momentum, it can perform multiple loops within the central detector, and thus produce more than eight hits. These cases are not treated separately, so several individual tracks can be reconstructed for one electron. This issue can be solved by including timing information from the fiber detector. Currently this is implemented by assigning those fiber hits to a short 4-hit track that are closest to the trajectory in the transverse plane. When two short tracks are combined to a long 8-hit track, the time difference and distance along the trajectory between the fiber hits is used to determine the correct flight direction and thus the charge of the electron as shown in figure 6.6a. Figure 6.6b illustrates how the timing information can also be used to calculate the speed of the particle and thus prevent the combination of short tracks from different loops.

The timing information provided by the tile detector, which has higher resolution as it is not required to be thin, can only be combined with long 6-hit tracks hitting the recurl stations. It will be used together with the fiber detector information to estimate time coincidence of different tracks at the vertex and thus, suppress combinatorical background.

The studies conducted in the scope of this thesis do not use time information. Including this is the logical next step to improve the reconstruction.

## 6.4. Computing Performance

For 3 layers, the number of triplets that have to be fitted scales with $n^3$. With typically $n = 10$ hits per layer this gives rise to $10^3$ combinations per frame or $2 \times 10^{10}$ combinations per second. Even though the triplet fit can be implemented

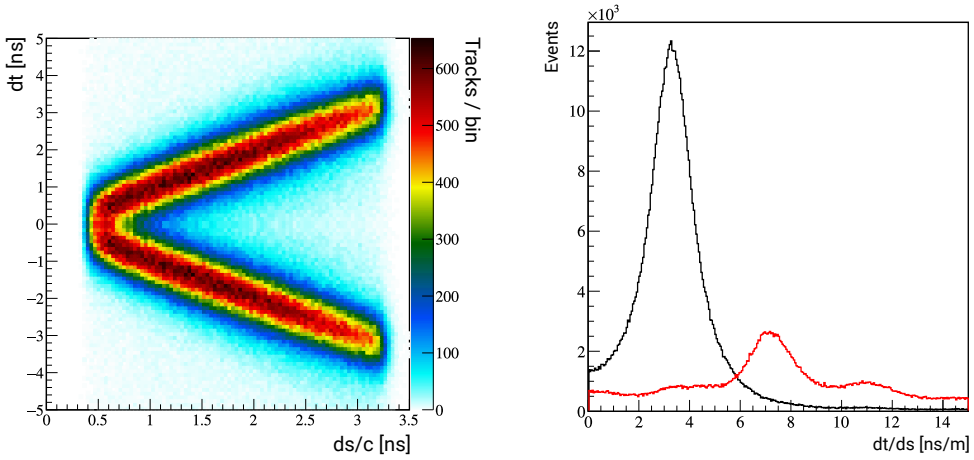


**(a)** Time difference $dt$ over distance along the trajectory $ds$ between fibre hits assigned to the two 4-hit tracks that are combined to a long 8-hit track. The upper branch indicates positive time differences, thus corresponds to to a track with correctly reconstructed flight direction and charge.

**(b)** The time difference and distance along the trajectory between fibre hits of an 8-hit track is used to estimate the particle's speed. For incorrectly combined 4-hit tracks from different loops (red line), the speed is larger than the speed of light, which is seen for true tracks (black line). The tails are due to time resolution of the fiber tracker.

**Figure 6.6.:** The timing information from the fiber detector can be used to reduce incorrectly reconstructed long 8-hit tracks. These plots show simulated data.

in parallel, it is still desirable to improve computing performance. In order to do this, some constraints on the combination of hits are applied. Only hits within a certain range in $\varphi$ and $z$ around the previous hit are considered in the fit. These ranges are determined empirically, resulting in $\mathrm{d}\varphi = 0.8\,\mathrm{rad}$ and $\mathrm{d}z = 20\,\mathrm{cm}$ for the first two hits. From the fourth hit onward, the track is propagated to the next layer for each additional hit. This reduces the search windows to $\mathrm{d}\varphi = 0.35\,\mathrm{rad}$ and $\mathrm{d}z = 10\,\mathrm{cm}$ between the second and the third layer and $\mathrm{d}\varphi = 0.035\,\mathrm{rad}$ and $\mathrm{d}z = 0.3\,\mathrm{cm}$ between the very closely spaced first and second, and third and fourth layers.

## 6.5. Extension to 5- and 7-Hit Tracks

The algorithm described so far requires at least one hit in every pixel layer. This demand is motivated by electrons originating from muon decays in the target region. Electrons from photon conversion, however, can have a vertex outside the first layer as photons can traverse matter without interacting. Therefore, in the scope of this

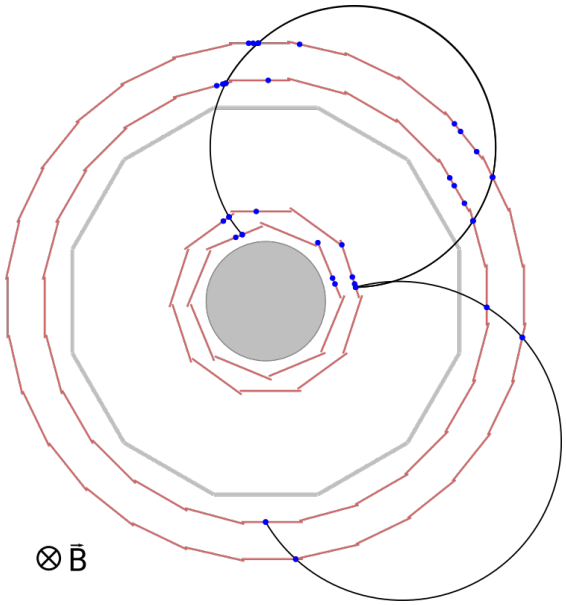


**Figure 6.7.:** Transverse view of the detector with pixel hits (blue), a 5-hit track from an electron and a 7-hit track from a positron. Both tracks have their first hit in the second layer.

thesis, the implementation is extended in a first step to also reconstruct tracks without a hit in the first layer. Analogous to the method described in chapter 6.1, outer triplets are fitted starting with hits in the second layer. In order to reduce the possible hit combinations, the outer triplets are fitted after the reconstruction of 4-hit tracks, so hits assigned to these are not used twice. This improves the computing performance and avoids fitting outer triplets from tracks that have a hit in the first layer. In order to reduce the number of false reconstructions, triplets with $\chi^2 > 50$ are rejected. Details of the analysis performed to choose this cut are described in chapter 7.1.1.

Additionally, it is possible to place a cut on the elevation angle $\lambda$ to exclude highly transverse tracks that loop many times in the central detector. These are very difficult to reconstruct due to the large number of hits and the small distances in between. The methods used to determine this cut is described in chapter 7.1.2.

The triplets that fulfill all criteria are saved. They are used as the basis to fit 5-hit tracks, analogous to the long 6-hit tracks, by using hits from the recurling electron. If the particle recurls in the central detector, a 7-hit track can be reconstructed by adding two additional hits from the vertex layers. Both cases are shown in figure 6.7. The cuts that are placed on these tracks are analyzed in chapter 7.1.

# 7. Photon Conversion Studies

This thesis presents preliminary studies on photon conversion events for the *Mu3e* detector. It concentrates on the track reconstruction of $e^+e^-$ pairs from a common vertex inside or below the second pixel layer. As the standard track reconstruction for *Mu3e* requires one hit in all four pixel layers, the algorithm has to be extended to include displaced vertices as described in chapter 6.5.

## 7.1. Track Selection

The studies presented in this chapter are conducted with photons from the simulated photon gun, as described in chapter 4.3.3, with energies in the range $10\,\text{MeV} < E_\gamma < 55\,\text{MeV}$. The lower limit is due to the detector acceptance for a conversion electron with almost the entire photon energy and a highly transverse momentum. The maximal energy of a photon radiated off the muon is half the muon mass. For these studies there is no muon beam, thus the detected electrons stem dominantly from photon conversion with some background contributions from Bhabha and Compton scattering.

### 7.1.1. Track Quality

Before any performance studies of the track reconstruction can be conducted, the selection criteria have to be chosen to achieve a large reduction of falsely reconstructed tracks, in the following called 'fakes', without losing too many correctly reconstructed tracks, called 'true tracks'. In the scope of this analysis, true tracks are the desired signal, while fake tracks constitute the background. Reconstructed tracks are determined as 'true' or 'fake' by using information from the Monte-Carlo simulation.

In addition to the geometrical factors described in chapter 6.1, the $\chi^2_{\text{min}}$ value from equation 5.20, provided by the fit algorithm for every track, is the main selection criterion. It describes the quality of a track fit and is distributed depending on the number of degrees of freedom of the track. The maximal $\chi^2$ value a track may have to still be saved, is called the cut value. It is chosen by considering two variables, the first of which is the signal efficiency:

$$\varepsilon(\chi^2_{\text{max}}) = \frac{S_{\text{cut}}(\chi^2_{\text{max}})}{S_{\text{total}}}, \qquad 0 \leq \varepsilon \leq 1. \tag{7.1}$$

$S_{\text{total}}$ is the number of all true tracks of a data set and $S_{\text{cut}}(\chi^2_{\text{max}})$ is the number of true tracks after eliminating tracks with $\chi^2 > \chi^2_{\text{max}}$.

The second variable is the purity, defined as

$$P(\chi^2_{\text{max}}) = \frac{S_{\text{cut}}(\chi^2_{\text{max}})}{S_{\text{cut}}(\chi^2_{\text{max}}) + B_{\text{cut}}(\chi^2_{\text{max}})}, \qquad 0 \leq P \leq 1. \tag{7.2}$$

Here, it gives a measure on the fraction of true tracks in a data set. Both of these variables should be maximized to find a good cut.

A third variable to describe the goodness of a cut is the background rejection:

$$R(\chi^2_{\text{max}}) = \frac{B_{\text{total}} - B_{\text{cut}}(\chi^2_{\text{max}})}{B_{\text{total}}}, \qquad 0 \leq R \leq 1, \tag{7.3}$$

giving the factor by which the fake tracks are reduced for a cut at $\chi^2 = \chi^2_{\text{max}}$. $B_{\text{cut}}$ and $B_{\text{total}}$ are the number of fake tracks with and without a cut, respectively.

### First Triplet

The first cut is placed on the $\chi^2$ value of the first triplet, made from hits in the second, third and fourth layers. In this case, the cut value is chosen with the aim to reduce the signal efficiency by no more than 1 %. Maximizing the purity is not the main objective, as the first triplet is not saved in itself but used to make longer tracks. The cut is therefore placed at $\chi^2 = 50$, as illustrated in figure 7.1a. This results in a background reduction by almost a factor of three (see table 7.1), comparable to the cut on the first triplet of the 4-hit track reconstruction.

The decision not to save triplets separately is based on the fact that three hits do not constrain a track enough to achieve the required precision in the reconstruction. This is indicated by the fake rate of 77 %. Including these tracks in the vertex reconstruction would significantly increase the combinatorical background.

### 5- and 7-Hit Tracks

With the $\chi^2$ cut on the first triplet in place, the optimal cut on the $\chi^2$ value of 5- and 7-hit tracks has to be found. Here, the aim is to maximize the purity of the data set without losing too much signal efficiency. Thus, the cut is chosen such that the product of purity and efficiency is maximized. This is shown in figures 7.2a and 7.3a, while figures 7.2b and 7.3b show the resulting background reduction. In the case of 5-hit tracks, the chosen cut of $\chi^2_{\text{5-hit}} = 13$ reduces the fake tracks by $R_{\text{5-hit}} = 93\,\%$, while maintaining the signal efficiency at $\varepsilon_{\text{5-hit}} = 93\,\%$. This results in a purity of $P_{\text{5-hit}} = 71\,\%$.

For 7-hit tracks, a background reduction of $R_{\text{7-hit}} = 99\,\%$ at signal efficiency $\varepsilon_{\text{7-hit}} = 87\,\%$ and purity $P_{\text{7-hit}} = 70\,\%$ percent is achieved with the cut placed at $\chi^2_{\text{7-hit}} = 22$. The much larger amount of fake tracks compared to 5-hit tracks is due to the fact that there are more hits in the vertex layers than in the recurl stations

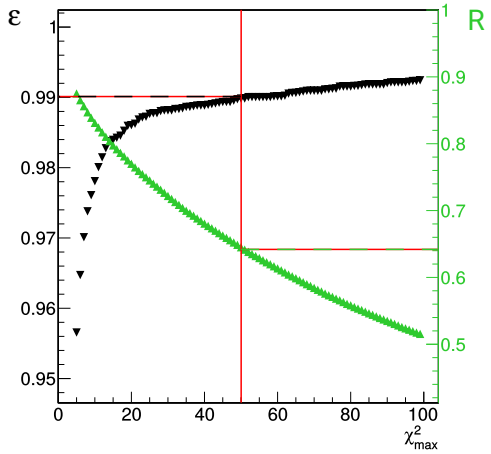


**(a)** The black line shows the signal efficiency $\varepsilon$ as defined in equation 7.1, while the green line shows the rejection of fake tracks $R$ according to equation 7.3. The chosen cut reduces fakes by 65 %, at an efficiency of 99 % with regard to true triplets.

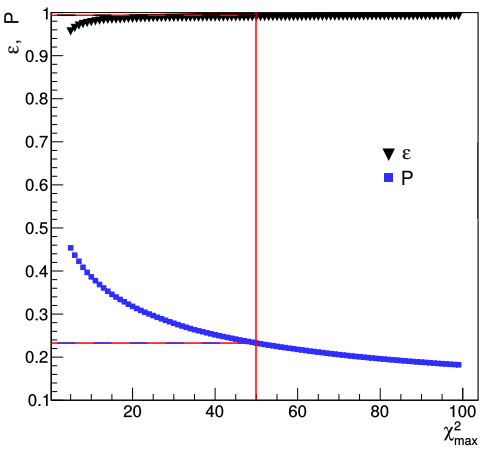


**(b)** Even though the background is reduced significantly, the purity $P$ (purple) of triplets in the sample is only 23 %.

**Figure 7.1.:** Analysis of the cut at $\chi^2 = 50$ (red) on the **first triplet** with a data set containing $\mathcal{O}(10^5)$ reconstructed triplets.

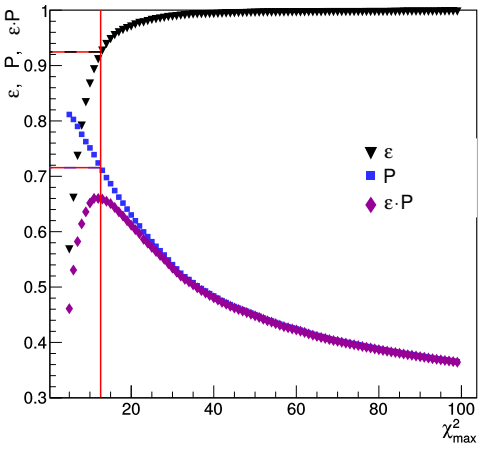


**(a)** Signal efficiency $\varepsilon(\chi^2_{\text{max}})$ (black) as defined in equation 7.1 and purity $P(\chi^2_{\text{max}})$ (blue) from equation 7.2 for $\chi^2$ cuts between 5 and 100. The point where $\varepsilon \cdot P$ (purple) reaches its maximum, identifies the optimal cut value. Here, $\chi^2_{\text{cut}} = 13$ (red) leads to an efficiency of $\varepsilon = 93\,\%$ at a purity of $P = 71\,\%$.

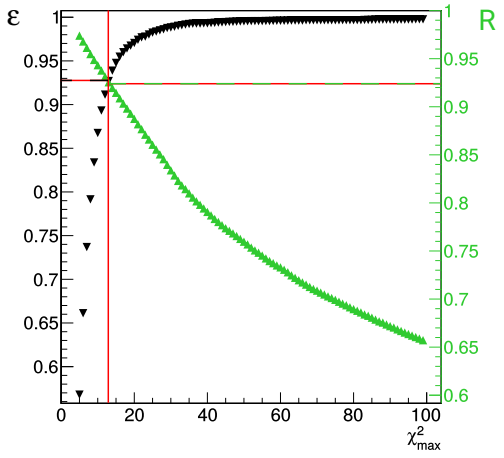


**(b)** In addition to the signal efficiency $\varepsilon$ (black), the background suppression rate $R$ is shown in green. The chosen $\chi^2$ cut (red) reduces the number of fake tracks by $R = 92.5\,\%$.

**Figure 7.2.:** Analysis of the $\chi^2$ cut on reconstructed **5-hit tracks**. This is conducted with a data set containing $5 \times 10^4$ reconstructed 5-hit tracks.

and therefore more fake tracks are fitted. After the cut is applied, the purity is almost the same as for 5-hit tracks, although it is not as efficient.

The results of the cut analysis are summarized in table 7.1. The resulting $\chi^2$ distributions for all tracks can be found in the appendix A.4.

### 7.1.2. Further Cuts

When an electron carries high transverse momentum, it can perform several turns in the central detector, producing multiple hits in all four pixel layers. In the following, these electrons will be called 'loopers'. They produce many closely spaced hits, leading to the reconstruction of tracks combining hits from different turns. One such event is shown in figure 7.4. A significant portion of fake tracks that cannot be eliminated with a $\chi^2$ cut stem from these events. The reconstruction generates an additional variable from the hit ID[1] of a track's first hit to identify the track corresponding to the electron's first loop inside the detector. Only this

[1]The track and hit information obtained from the simulation is explained in chapter 4.3.4.

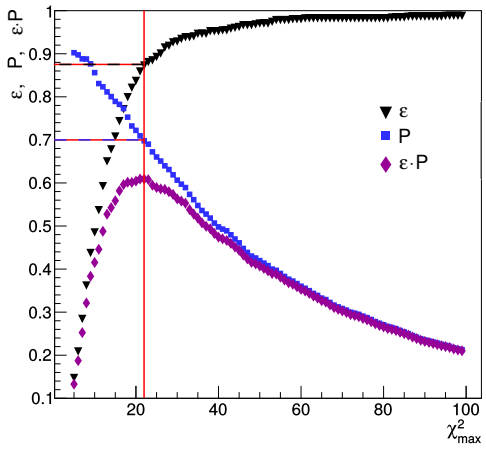


**(a)** Signal efficiency $\varepsilon(\chi^2_{\text{max}})$ (black) as defined in equation 7.1 and purity $P(\chi^2_{\text{max}})$ (blue) from equation 7.2 for $\chi^2$ cuts between 5 and 100. The point where $\varepsilon \cdot P$ (purple) reaches its maximum, identifies the optimal cut value. Here, $\chi^2_{\text{cut}} = 22$ (red) leads to an efficiency of $\varepsilon = 87\,\%$ at a purity of $P = 70\,\%$.

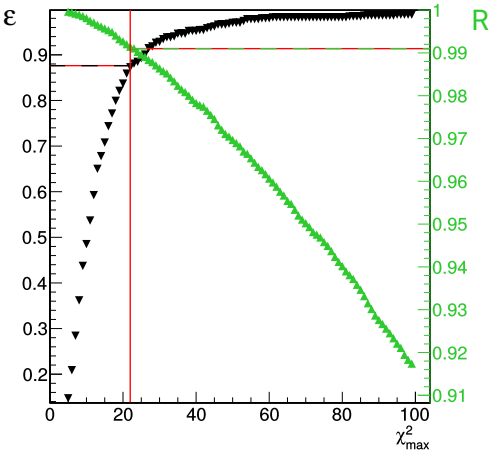


**(b)** In addition to the signal efficiency $\varepsilon$ (black), the background suppression rate $R$ is shown in green. The chosen cut at $\chi^2_{\text{cut}} = 22$ (red) reduces the number of fake tracks by $R = 99.1\,\%$. The large reduction is due to the large number of fake tracks fitted to the numerous hits in the vertex layers.

**Figure 7.3.:** Analysis of the $\chi^2$ cut on reconstructed **7-hit tracks**. This is conducted with a data set containing $2 \times 10^4$ reconstructed 7-hit tracks.

**Table 7.1.:** $\chi^2$ cut and resulting values for the true track efficiency $\varepsilon$, the purity of the data set $P$ and the factor of fake track reduction $R$.

| | $\chi^2_{\text{cut}}$ | $\varepsilon$ | $P$ | $R$ |
|---|---|---|---|---|
| $1^{st}$ triplet | 50 | 99 % | 23 % | 65 % |
| 5-hit tracks | 13 | 93 % | 71 % | 93 % |
| 7-hit tracks | 22 | 87 % | 70 % | 99 % |

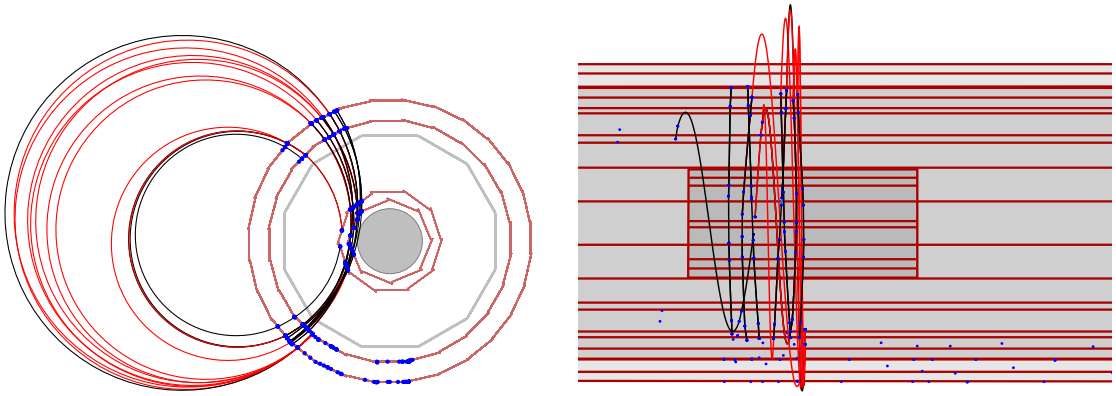

**(a)** Transverse view of the detector. The decreasing radius of the trajectory illustrates the energy loss of the looper at every turn.

**(b)** Longitudinal view. The hits produced by the second particle (blue dots in the lower right part) clearly show the trajectory although there are no reconstructed tracks.

**Figure 7.4.:** Cross section of the detector with a looping particle. true tracks are shown in black and fakes in red. Here, the looper belongs to an asymmetric conversion pair. The second particle with small momentum is looping in the third and fourth layer. No tracks are reconstructed, as there are no hits in the vertex layers, but the pixel hits (blue dots) are clearly visible in the bottom part.

first loop can be used to reconstruct an interaction vertex but multiple loops are reconstructed as separate tracks.

The easiest way to eliminate loopers, is to require a minimum for the elevation angle $\lambda_1$ of the particle's momentum at the first hit. Such a cut has been used in the first development stages of the extension that includes 5- and 7-hit tracks into the reconstruction (see appendix A.3). For the studies presented here however, this cut has been lifted, because while it reduces the background significantly, it also eliminates a large number of true tracks. If loopers are required to be eliminated for an analysis in the future, it can easily be included again.

## 7.2. Momentum Resolution

In order to evaluate the momentum resolution for the different types of reconstructed tracks, the difference between the reconstructed momentum $p_{\text{track}}$ and the simulated momentum $p_{\text{MC}}$ is fitted with a Gaussian, giving the resolution as the standard deviation $\sigma_p$. This is only possible for the core of the distribution, as there is a tail towards low momenta. The tail is caused by the fact that $p_{\text{MC}}$ is the particle's momentum at the first hit, while $p_{\text{track}}$ includes a simplified energy loss correction. This is implemented as the most probable energy loss per layer and does not fully reflect the exact distribution of energy loss through Bremsstrahlung, which is the most dominant process. The Landau distribution in figure 5.2 shows the tail

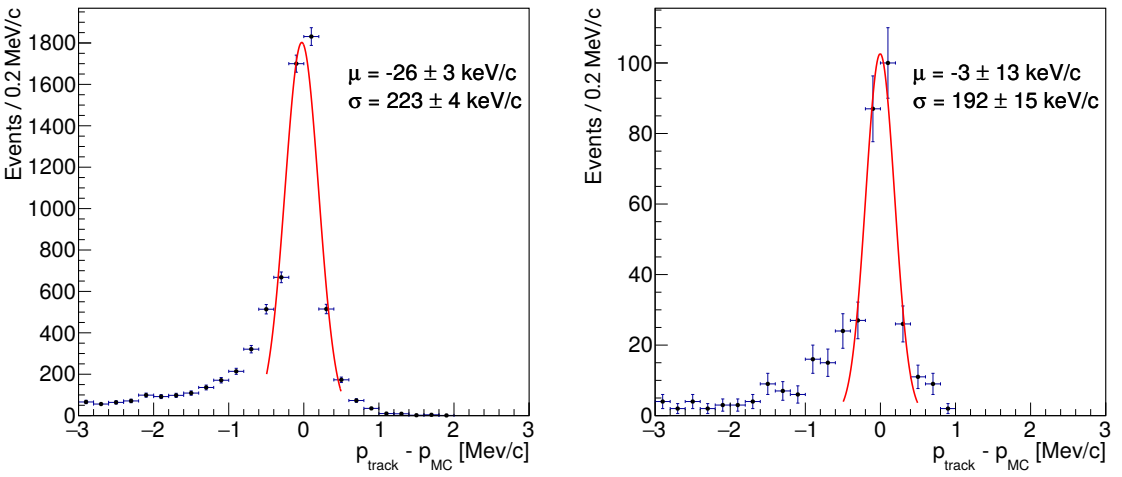


**(a)** The momentum resolution for **5-hit tracks** is $\sigma_p \approx 0.22\,\mathrm{MeV}/c$. Conducted with a data set of size $8 \times 10^3$.

**(b)** The momentum resolution for **7-hit tracks** is $\sigma_p \approx 0.19\,\mathrm{MeV}/c$. The large error bars are due to the smaller sample size of 440 tracks.

**Figure 7.5.:** The difference between the reconstructed momentum $p_{\mathrm{track}}$ and the simulated momentum $p_{\mathrm{MC}}$. The core of the distribution is fitted with a Gaussian, giving the momentum resolution $\sigma_p$. The tail towards lower momenta is due to the way energy loss is implemented.

towards higher energy losses, that is not corrected for in the reconstruction. The distribution of $p_{\mathrm{track}} - p_{\mathrm{MC}}$ for 5- and 7-hits is shown in figure 7.5. Momentum resolutions of $\sigma_{p,\text{5-hit}} = 0.223(4)\,\mathrm{MeV}/c$ and $\sigma_{p,\text{7-hit}} = 0.192(15)\,\mathrm{MeV}/c$ are achieved.

In addition, it is interesting to investigate the dependence of the momentum resolution on the momentum itself. In order to illustrate the dependence, the resolution is plotted against different momenta. The plots are shown in figure 7.6.

## 7.3. Performance Studies

In order to assess the quality of the reconstruction of 5- and 7-hit tracks originating outside the first layer, the achieved momentum resolution is compared to 6- and 8- hit tracks from within the first layer (see plots in figures A.8b and A.9b). The results are summarized in table 7.2. The table also shows the resolution of 4-hit tracks (see figure A.10) for comparison. It is significantly worse than for long tracks as the tracks have not yet recurled.

In conclusion, these studies show that the track reconstruction of 5- and 7-hit tracks performs as well as in the presence of an additional hit from the first pixel layer.

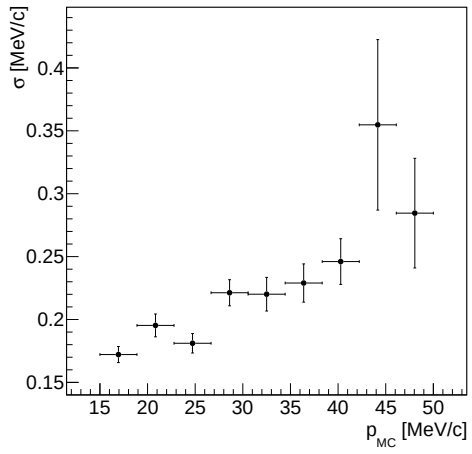


**(a)** $8 \times 10^3$ **5-hit tracks** with $15\,\mathrm{MeV}/c < p_{\mathrm{MC}} < 50\,\mathrm{MeV}/c$ in bins of $4\,\mathrm{MeV}/c$.

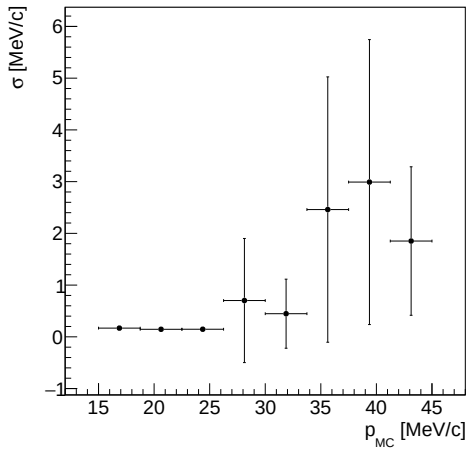


**(b)** 440 **7-hit tracks** with $15\,\mathrm{MeV}/c < p_{\mathrm{MC}} < 45\,\mathrm{MeV}/c$ in bins of $4\,\mathrm{MeV}/c$. There are only few tracks at $p_{\mathrm{MC}} > 25\,\mathrm{MeV}/c$, as there are only few large momentum tracks that recurl in the central detector (see Appendix A.7).

**Figure 7.6.:** Fitted momentum resolution $\sigma_p$ as a function of the true momentum $p_{\mathrm{MC}}$.

**Table 7.2.:** The momentum resolution $\sigma_p$ of tracks originating in the second layer compared to that of tracks originating in the first layer.

| $\sigma[\mathrm{MeV}/c]$ | $1^{\mathrm{st}}$ layer | $2^{\mathrm{nd}}$ layer |
|---|---|---|
| 5-hit tracks | - | 0.223(4) |
| 6-hit tracks | 0.216(3) | - |
| 7-hit tracks | - | 0.192(15) |
| 8-hit tracks | 0.193(5) | - |
| 4-hit tracks | 1.54(1) | - |

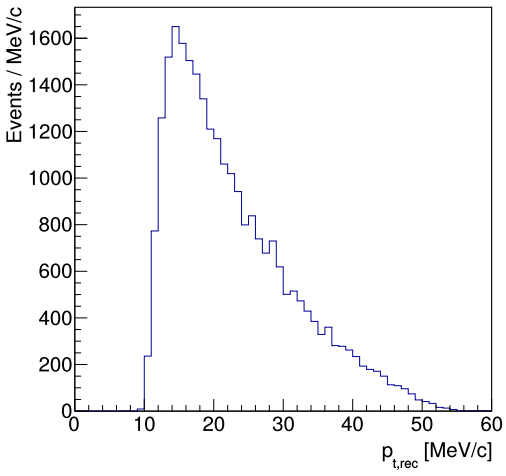


**Figure 7.7.:** The transverse momentum distribution of all (5-, 6-, 7- and 8-hit) reconstructed true tracks corresponding to the first loop of a particle. The low-momentum cut-off gives the minimal $p_t$ a particle requires to be reconstructable.

#### Momentum Distribution

In order to see the difference in acceptance between tracks from the first and tracks from the second pixel layer, the reconstructed transverse momentum $p_{t,\mathrm{rec}}$ is considered:

$$p_{t,\mathrm{rec}} = p_{\mathrm{rec}} \cos\lambda. \tag{7.4}$$

The lower limit of $p_{t,\mathrm{rec}}$ gives the minimal transverse momentum a particle requires to reach the outermost layer and thus, to be reconstructed. Figure 7.7 shows the transverse momentum for all reconstructed tracks that correspond to the first loop of a particle. There is a cut-off at the minimal $p_t$ a particle requires to be reconstructable. For 6- and 8- hit tracks the minimal transverse momentum is $\mathrm{Min}(p_{t,\mathrm{rec,\ 6,8\text{-}hit}}) \approx 10.5\,\mathrm{MeV}/c$, while tracks from the second layer can be reconstructed with a minimal transverse momentum of $\mathrm{Min}(p_{t,\mathrm{rec,\ 5,7\text{-}hit}}) \approx 9\,\mathrm{MeV}/c$. The difference in the acceptance of low transverse momentum tracks is as small as expected, due to the small radial distance between the first and second pixel layer of less than 7 mm.

### 7.3.1. Vertex Reconstruction and Acceptance

The data set, which is used for these studies, contains $10^7$ generated photons. Of these, 0.05 % convert to an $e^+e^-$ pair in the target region, the first, or the second pixel layer, and produce a track within the geometrical acceptance and with the required minimal transverse momentum.

**Table 7.3.:** Contributions to the reconstruction of **photon conversion events**, which produce $e^+e^-$ pairs within the acceptance range, of tracks from the first layer are compared to contributions from tracks from the second layer.

| | $1^{st}$ layer | $2^{nd}$ layer | Total |
|---|---|---|---|
| Tracks | 49 % | 39 % | 88 % |
| Vertex | 25 % | 16 % | 41 % |

When considering only tracks with a hit in the first pixel layer, 49 % of the tracks within the acceptance range are reconstructed correctly. Including the reconstruction of 5- and 7-hit tracks increases the acceptance for tracks from displaced vertices, as all tracks that do not produce a hit in the first pixel layer would otherwise be lost. Thus, the total number of reconstructed tracks increases by approximately 80 % when 5- and 7- hit tracks are included.

In total, 88 % of tracks within the acceptance region are reconstructed correctly.

The reconstruction of vertices from $e^+e^-$ pairs is performed using the vertex fit for photon conversion events described in chapter 5.2. Studies on vertex selection and purity are not yet undertaken. Therefore, only correctly reconstructed tracks corresponding to the first loop of an electron are in the following used to find vertices.

The extension of the track reconstruction allows for the reconstruction of vertices in the second pixel layer. The achieved gain in the total number of reconstructed vertices is expected to be lower than the gain in the number of reconstructed tracks. This is because both tracks of a conversion pair have to be fully reconstructed. It is notable, that all track pairs, for which a vertex can be reconstructed, originate in the same layer.

25 % of the vertices within the acceptance range are reconstructed from tracks originating in the first pixel layer. Including 5- and 7-hit tracks from the second pixel layer increases the number of reconstructed vertices by 62 %.

In total, 41 % of vertices within the acceptance range are reconstructed.

Table 7.3 summarizes the result of the reconstruction for the photon gun studies.

## 7.4. Material Mapping

As a first application, the extended track reconstruction algorithm is applied to Standard Model muon decays. The most straightforward use of the photon conversion reconstruction is the mapping of the material inside the detector. It can be employed within the scope of the current detector design. As the probability for a photon to convert into an $e^+e^-$ pair depends on the material it traverses (see chapter 2.2.2), the reconstruction of conversion vertices yields a map of the material distribution within the region of acceptance. Here, $e^+e^-$ pairs from Bhabha scattering are not a source of background but can also contribute to the material mapping. The background for material mapping stems from the radiative muon decay with internal conversion and from wrong combinations of $e^+e^-$ tracks.

With the extended track reconstruction presented in this thesis and the vertex reconstruction of photon conversion events described in chapter 5.2, vertices in the target region and the first and second pixel layers can be reconstructed. As explained in chapter 7.3.1, the vertex fit is conducted with correctly reconstructed tracks.

Considering only the Standard Model decays of the muon, photons originate from the radiative decay $\mu \to e\gamma\nu\nu$, shown in figure 2.2b, which has a branching ratio of $\mathcal{B} = 1.4(4)\,\%$. The material budget for the two inner layers is only $0.23\,\%$ $X_0$. This is slightly increased if the track angle is not perpendicular to the layer, but the conversion probability remains low. However, the high muon rate permits enough conversion event reconstructions to map the material distribution, especially if Bhabha events are included.

The following studies are conducted with a data set corresponding to a measuring time of 5 s at a muon rate of $1.9 \times 10^8$ muons/s. With 55 % of muons reaching the target at a stopping rate of 92 %, this corresponds to approximately $5 \times 10^8$ muons being stopped and decaying on the target.

In the following, only conversion pairs produced by photons from the $7 \times 10^6$ total radiative decays are considered. Out of these, approximately 0.05 % convert to an $e^+e^-$ pair in the target region, the first, or the second pixel layer, and produce at least one track within the geometrical acceptance and with the required minimal transverse momentum. For 48 % of the events within the acceptance a vertex is fully reconstructed, giving a total of $1.8 \times 10^3$ reconstructed photon conversion vertices.

In addition, $1.2 \times 10^6$ Bhabha vertices are reconstructed. The large amount of Bhabha tracks contributes dominantly to the combinatorical background of the vertex reconstruction. In order to reduce this background, Bhabha events are only included if the $\chi^2$ value from the vertex fit is smaller than 5. This cut is chosen to reduce the number of falsely reconstructed vertices by approximately 90 %. An additional reduction in fake vertices of approximately 68 % is achieved by requiring the invariant mass of the $e^+e^-$ pair to be between $5\,\mathrm{MeV}/c^2$ and $7.5\,\mathrm{MeV}/c^2$ [Ger17], as true Bhabha events lie within this range.

Figure 7.8 shows the reconstructed vertices in transverse and longitudinal view. The first and second layers, made up of 8 and 10 pixel ladders respectively, are well recognizable in the transverse view, as is the hollow double cone shape of the target

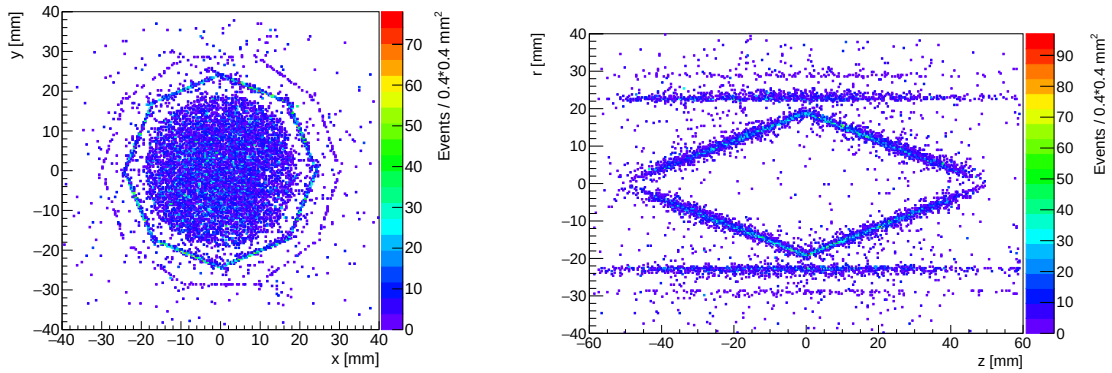


**(a)** Transverse view.

**(b)** Projection onto the $r$-$z$ plane. Vertices with $y < 0$ are projected onto $-r$.

**Figure 7.8.:** The reconstructed vertices of $e^+e^-$ pairs from Bhabha scattering and photon conversion yield a map of the material distribution inside the detector. The target, the first and the second pixel layer are visible. The vertices outside the material stem mainly from wrong combinations of Bhabha electrons. This map corresponds to 5 s of data taking time.

in the longitudinal view. The material map can be expected to be more detailed with a longer run time.

### 7.4.1. Background

The vertices lying outside the second pixel layer in figure 7.8 are due to combinatorical background. They can not correspond to a true vertex, as tracks originating outside the second layer are not reconstructed. In order to reduce this background and obtain clearer material mapping results, Bhabha events need to be eliminated to a higher degree. This can be achieved by requiring the invariant mass of the $e^+e^-$ pair to be smaller than $5\,\mathrm{MeV}/c^2$ [Ger17]. Figure 7.9 shows a map containing only the reconstructed photon conversion vertices from this data set. Studies on background suppression have to be extended to achieve comparable results using only the reconstructed track parameters without additional information from the simulation. First results with a cut on Bhabha events at $m_{\mathrm{inv}} = 5\,\mathrm{MeV}/c^2$ are shown in figure A.11.

The studies above have been conducted using information from the simulation to eliminate all undesired events. Apart from Bhabha events, there are other processes supplying electrons and positrons that contribute to the combinatorical background. In this data sample, which contains $5 \times 10^8$ stopped muons, there are $3 \times 10^6$ fully reconstructed $e^+e^-$ vertices. They stem from combinations of electrons and positrons from different processes like Michel decays, radiative decays with and

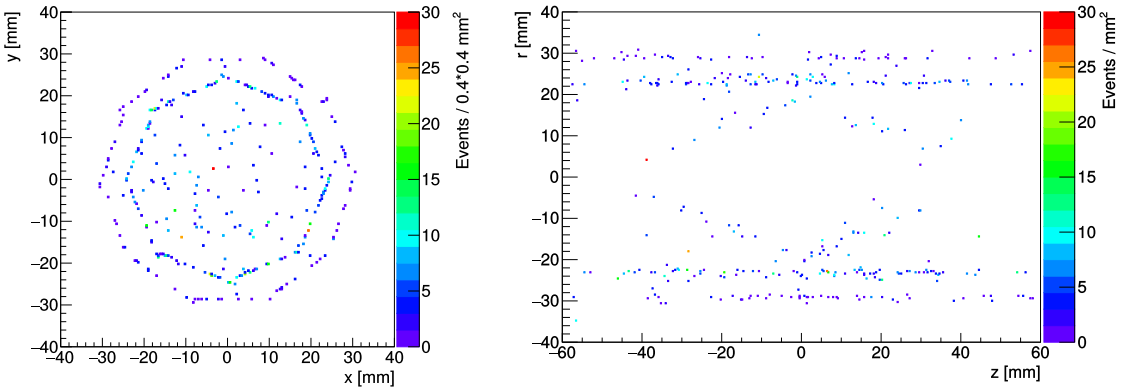


**(a)** Transverse view.

**(b)** Projection onto the $r$-$z$ plane. Vertices with $y < 0$ are projected onto $-r$.

**Figure 7.9.:** The reconstructed vertices of photon conversion events yield a clear map of the material distribution inside the detector. Here, $1.8 \times 10^3$ vertices from conversion in the target region, in the first, or in the second pixel layer are shown. This corresponds to 5 s of data taking time.

without internal conversion, Bhabha and Compton scattering and Photon conversion. Figure 7.10 shows the origin of electrons and positrons that are combined to $e^+e^-$ pairs. The fraction of correctly reconstructed photon conversion events is 0.06 %. Conversion electrons are often paired with a wrong positron as there is a large number of them available from the muon decay.

In order to produce a material map of the detector from measured data, the background has to be controlled. Most wrong combinations should be eliminated by including timing information and with appropriate cuts on the $\chi^2$ value of the vertex fit and the invariant mass of the $e^+e^-$ pair. Further studies are required to chose these cuts and optimize the vertex selection process.

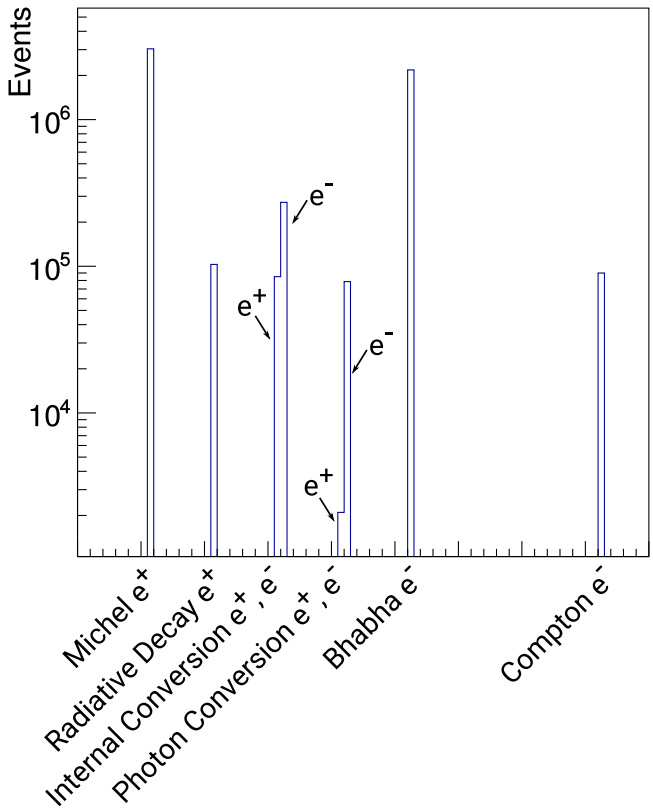


**Figure 7.10.:** Origin of particles that can be combined to $e^+e^-$ pairs from simulating 5 s of Standard Model processes at a rate of $10^8$ stopped muons/s. Here, there are no cuts on the vertex reconstruction.

**Table 7.4.:** Simulated dark photons with $\epsilon^2 = 10^{-9}$ for different masses $m_{A'}$, with corresponding lifetimes $\tau_{A'}$ (see equation 2.7). The momenta are estimated from the peak position of the simulated momentum distribtion, and give the flight distances $L_{A'}$ (see equation 7.5).

| $m_{A'}$ [MeV/$c^2$] | $\tau_{A'}$ [ps] | $p_{A'}$ [MeV/$c$] | $L_{A'}$ [mm] |
|---|---|---|---|
| 10 | 26.7 | 18 | 14.4 |
| 20 | 13.3 | 24 | 4.8 |
| 30 | 8.9 | 25 | 2.7 |
| 40 | 6.7 | 27 | 1.4 |
| 50 | 5.3 | 26 | 0.83 |
| 60 | 4.4 | 23 | 0.50 |
| 70 | 3.8 | 20 | 0.31 |
| 90 | 3.0 | 9 | 0.09 |
| 100 | 2.7 | 4 | 0.03 |

## 7.5. Dark Photons

First studies are conducted on the reconstruction of dark photon decays from displaced vertices. These are based on the simulation of one muon decay per simulation time frame, radiating a dark photon with a finite lifetime, which decays into an $e^+e^-$ pair: $\mu^+ \to \overline{\nu}_\mu \nu_e e^+ A'$ with $A' \to e^+e^-$. The dark photon mass $m_{A'}$ and the lifetime $\tau_{A'}$ can be chosen in the simulation. Firstly, the simulated tracks are reconstructed using the extended track reconstruction to include decays outside the first pixel layer, and then the conversion vertex reconstruction is performed.

The colored lines in figure 3.2a show the square of the mixing parameter $\epsilon^2$ as a function of $m_{A'}$ for different flight distances in the mass range between 10 and 100 MeV/$c^2$, which is accessible in muon decays. In this study dark photons with $\epsilon^2 = 10^{-9}$ are investigated. This gives flight distances in the order of 10 µm to 10 mm in an, as of yet, not excluded range. Table 7.4 lists the dark photon masses and the corresponding lifetimes $\tau_{A'}$ (according to equation 2.7) for the simulations presented here. It further includes the most probable momentum $p_{A'}$ of the dark photon, estimated from the peak position of the simulated momentum distribution, and the corresponding flight distance

$$L_{A'} = c\tau_{A'} \cdot \beta\gamma, \text{ with } \beta\gamma = \frac{p_{A'}}{m_{A'}c}. \tag{7.5}$$

The reconstructed invariant mass $m_{\text{inv}}$ of the reconstructed $e^+e^-$ pair for all simulated dark photon masses is shown in figure 7.11a. The data sets contain $10^4$ dark photon decays each. Decay electrons from dark photons with low masses carry lower momenta and are therefore more often not within the acceptance range.

**Table 7.5.:** Efficiencies $\mathcal{E}$ of the full reconstruction of dark photons with different masses $m_{\mathrm{A}'}$. For each datasample $10^4$ dark photons are generated.

| $m_{\mathrm{A}'}$ [MeV/$c^2$] | $\mathcal{E}$ |
|---|---|
| 10 | 5.3 % |
| 20 | 10.3 % |
| 30 | 27.7 % |
| 40 | 53.9 % |
| 50 | 71.0 % |
| 60 | 76.1 % |
| 70 | 69.6 % |
| 90 | 58.7 % |
| 100 | 46.9 % |

Very high mass dark photons carry only small momenta and therefore produce $e^+e^-$ pairs with a large opening angle of almost 180°. Vertices from such events are difficult to reconstruct as the tracks are close to parallel at every point. Thus, the highest reconstruction efficiencies can be achieved for dark photon masses of around 60 MeV/$c^2$. All reconstruction efficiencies for the investigated dark photon masses are given in table 7.5.

The invariant mass $m_{\mathrm{inv}}$ of the reconstructed $e^+e^-$ pair for all reconstructed vertices can be fitted with a Gaussian distribution, giving the mass resolution $\sigma_m$. The achieved result is comparable for all chosen masses and the combined resolution of $\sigma_m = 0.7\,\mathrm{MeV}/c^2$ is shown in figure 7.11b.

These studies are performed on simulated data sets containing only signal decays. In order to conduct dark photon searches on measured data, the background has to be considered. Here the main background sources are Bhabha scattering and photon conversion. Both of these can be excluded by requiring a minimum on the invariant mass of of the reconstructed $e^+e^-$ pair. Furthermore, the background processes only take place within the material, while dark photons can decay anywhere. If the material distribution within the detector is known, the search can be confined to regions with less material, for example between the target and the first pixel layer or between the detection layers. Although this method would reduce background from Bhabha and photon conversion events, it also decreases the sensitivity as the acceptance region is constricted. Combinatorical background can only be reduced by including timing information and requiring both tracks to be coincident in time. In order to evaluate the sensitivity the *Mu3e* experiment can achieve, detailed studies on the background and the attainable vertex resolution have to be undertaken.

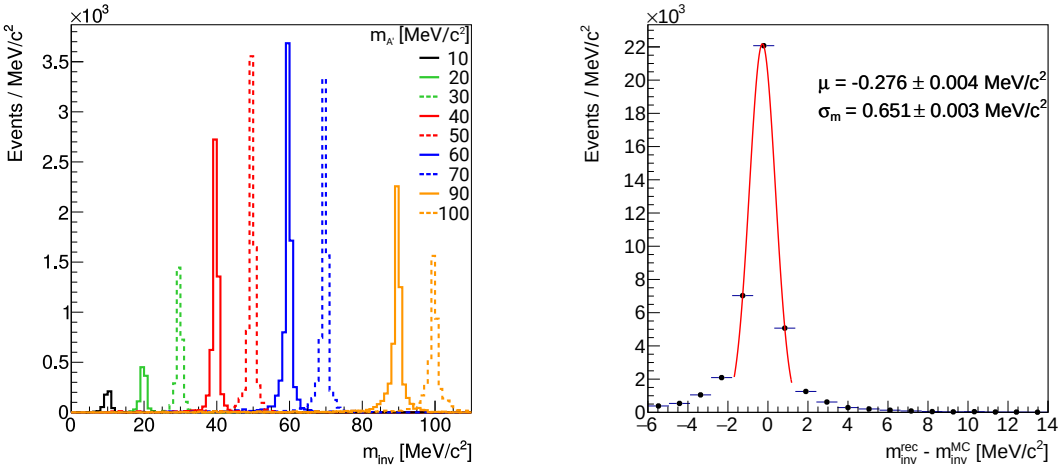


**(a)** The reconstructed invariant mass $m_{\text{inv}}$ of the reconstructed $e^+e^-$ pair for different simulated dark photon masses. Each data sample contains $10^4$ simulated dark photons.

**(b)** The resolution of the invariant mass $m_{\text{inv}}$ of $4.2 \times 10^4$ reconstructed $e^+e^-$ pairs from a total of $9 \times 10^4$ dark photon decays. The average resolution is $\sigma_m = 0.7\,\text{MeV}/c^2$.

**Figure 7.11.:** Reconstructed dark photon decays for $\epsilon^2 = 10^{-9}$ and masses accessible in the muon decay.

# 8. Conclusion and Outlook

The *Mu3e* collaboration, searching for the lepton flavor violating decay $\mu^+ \to e^+e^-e^+$, is designing a detector that is optimized to track low-energy electrons in a multiple scattering dominated regime with high precision. In order to search for the rare signal event with a sensitivity down to 1 in $10^{16}$ decays, the background suppression has to be sufficiently large, requiring an average momentum resolution of 0.3 MeV/$c$. This is achieved with a cylindrically symmetric design of four thin silicon pixel layers of 0.115 % $X_0$ thickness each for electron tracking. The pixel layers are arranged in pairs at radii of approximately 25 mm and 80 mm. The outer two layers have a total length of approximately 1.2 m, allowing electrons bending in the magnetic field to re-enter the tracking layers and produce more than four hits. In addition to high-precision reconstruction, the *Mu3e* detector is able to deal with high particle rates, which makes it possible to use it for further measurements and searches. Potential applications are for example the search for dark photons A′ in decays like $\mu^+ \to e^+\overline{\nu}_\mu\nu_e$A′, followed by A′ $\to e^+e^-$, for another lepton flavor violating decay $\mu^+ \to e^+\gamma$, or the precision measurement of the Dalitz decay of the pion $\pi^0 \to e^+e^-\gamma$. Measuring these processes requires the reconstruction of $e^+e^-$ pairs from displaced vertices, either from photon conversion events or from the decay of dark photons.

This thesis introduces the necessary extensions to adapt the *Mu3e* track reconstruction to conversion events inside the second pixel layer and gives an overview over the performance. Furthermore, it presents first studies from applying the algorithm to simulated Standard Model processes and dark photon decays. In this chapter, the results are summarized and discussed.

## 8.1. Summary and Discussion

The extended track reconstruction is developed and tested on a simulation of the *Mu3e* detector using photons from a photon gun. After the standard reconstruction of 4-, 6- and 8-hit tracks, originating inside the target region or the first pixel layer, is completed for one reconstruction frame, the remaining hits are used to fit 5- and 7- hit tracks in an analogous way, starting with hits in the second pixel layer. 3-hit tracks, the equivalent to 4-hit tracks without a hit in the first layer, are not saved separately. The weak constraints on the track fit from only three hits lead to a fake rate of 77 %, which would increase the background significantly.

Selection criteria for reconstructed tracks are optimized to maximally reduce the fraction of falsely reconstructed tracks without loosing too much efficiency in true

tracks. For 5-hit tracks, the background is reduced by 92.5 % at an efficiency of 93 %. This results in 71 % true 5-hit tracks in the data sample. 7-hit tracks are reconstructed with 70 % true tracks, achieved by reducing the fake rate by 99 % at an efficiency of 87 %.

In order to evaluate the performance of the extended reconstruction, the momentum resolution of 5- and 7-hit tracks is compared to that of 6- and 8-hit tracks. The average resolution that can be reached is $\sigma_{5,7\text{-hit}} = 0.2\,\text{MeV}/c$, which is as good as the momentum resolution of 6- and 8-hit tracks $\sigma_{6,8\text{-hit}} = 0.2\,\text{MeV}/c$.

In conclusion, the photon gun studies show that, although 5- and 7-hit tracks originating in the second pixel layer are constrained by one hit less than 6- and 8-hit tracks, their reconstruction performs as well as the standard reconstruction. The extension improves the acceptance of events that produce particles from displaced vertices like photon conversion and the decay of dark photons with a finite lifetime.

However, less than 0.1 % of photon conversions within the geometrical and momentum acceptance range is not enough to search for rare processes involving photons. The *Mu3e* experiment requires a detector upgrade to achieve better sensitivities than experiments that are dedicated to measure photon conversion events. Suggestions for improvements are made in the next chapter.

As a first application of the extended reconstruction algorithm, Standard Model muon decays are investigated. Here, the total number of reconstructed vertices of photon conversion events increases by 13 % when 5- and 7- hit tracks are included, improving the acceptance of tracks from displaced vertices significantly. Performing a track and vertex reconstruction of $e^+e^-$ pairs from photon conversion events and Bhabha scattering produces a map of the material distribution within the detector. A clearer version is achieved when only photon conversion events are considered, as Bhabha scattering contributes dominantly to the combinatorical background. Simulating 5 s of run time at a stopping rate of $10^8$ muons/s shows, that the material mapping works in principle. In order to obtain a clear and detailed map of the material distribution, more data has to be analyzed, and the background from mismatched tracks needs to be controlled.

A preliminary study of dark photons that decay with a finite lifetime and thus produce displaced vertices, is conducted. Dark photons from the muon decay $\mu^+ \to \overline{\nu}_\mu \nu_e e^+ \text{A}'$, with masses between 10 and 100 $\text{MeV}/c^2$ and corresponding lifetimes between 27 and 3 ps are investigated. They have average flight distances between 14 and 0.03 mm. The reconstruction efficiency for $\text{A}' \to e^+e^-$ decays is maximal with 76 % for dark photon masses around 60 $\text{MeV}/c^2$. The track and vertex reconstruction of $e^+e^-$ pairs from the dark photon decay yields the expected invariant masses with an average resolution of $\sigma_m = 0.7\,\text{MeV}/c^2$. Further investigations should be made into the achievable vertex resolution depending on the flight distance. This study is performed on signal decays only. In order to evaluate the sensitivity the *Mu3e* experiment can achieve, studies on the background from photon conversion events, Bhabha scattering and combinatorics have to be undertaken.

## 8.2. Outlook

In order to conduct more detailed studies on the application of the *Mu3e* detector to precision measurements and searches for rare processes that involve displaced $e^+e^-$ vertices, the reconstruction has to be improved. A very important tool to exclude falsely reconstructed tracks are the timing detectors. Adding the information they provide to the reconstruction, allows for eliminating tracks that do not correspond to the first loop of a particle, charge misidentifications and for ensuring time coincidence at the vertex.

Considering the small distance between the first and the second pixel layer of approximately 7 mm, multiple scattering effects are low and the resulting uncertainty becomes comparable to the pixel size. The same is true for the outer two layers. Here, the track reconstruction should be adjusted to include the uncertainty due to pixel size.

With the current detector design, the most obvious area for improvement is the acceptance. While this thesis only discusses the extension to tracks originating in the second pixel layer, it might also be possible to reconstruct conversions in the outer layers. As this includes the fiber tracker, which has a significantly shorter radiation length than the pixel layers, it would clearly increase the acceptance for electrons from photon conversion events. The same is true for low momentum particles that only hit two layers (clearly visible in figure 7.4). The main problem in both cases is the small number of hits, namely four, with which to fit a track. This would result in an increased number of fake reconstructions and a decreased momentum resolution.

Apart from improvements in the track reconstruction, the vertex reconstruction has to be studied as well. Cuts on the $\chi^2$ value of the vertex fit and the invariant mass of the $e^+e^-$ pair have to be chosen to optimize the efficiency and purity of reconstructed vertices depending on the desired application to photon conversion events or dark photon decays.

The detector is designed to minimize the material budget, which is counterproductive to inducing photon conversions. However, measuring these is desired when searching for the decay $\mu^+ \to e^+\gamma$ or measuring the electromagnetic transition form factor in the decay $\pi^0 \to e^+e^-\gamma$. An updated design has been suggested by [Che+13]. It extends the *Mu3e* detector by a conversion layer, which could be realized as an additional timing detector, and two more pixel layers at a radius of approximately 20 cm. This is schematically shown in figure 3.1. Detailed studies have to be conducted to investigate the optimal set-up to increase the conversion rate while considering the increase in energy loss and multiple scattering.

With these modifications, the *Mu3e* detector might be well suited to improving several of the aforementioned measurements.

# A. Appendix

## A.1. Acceptance Angle

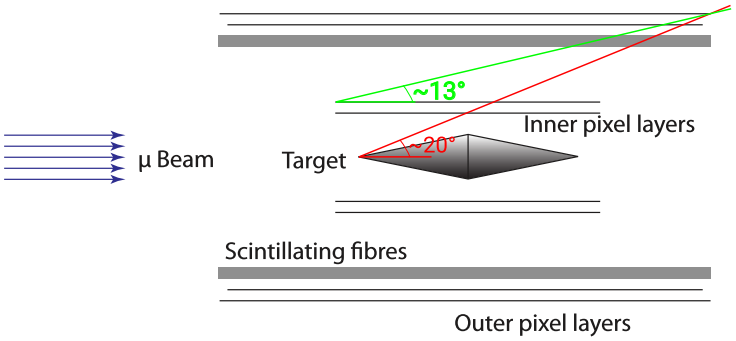


**Figure A.1.:** The minimal elevation angle for a particle originating from the target to be within the geometrical acceptance of the detector is approximately 20°. Low-momentum particles require a larger angle to be accepted due to stronger bending in the magnetic field. For electrons originating inside the vertex layers the geometrical acceptance improves with a minimal elevation angle of 13°.

## A.2. Momentum Resolution in a Multiple Scattering Dominated Detector

The standard deviation of the scattering angle for multiple scattering in material is given by the Highland formula

$$\sigma_{\mathrm{MS}} = \frac{13.6\,\mathrm{MeV}}{p\beta c} z \sqrt{\frac{x}{X_0}} \left(1 + 0.038 \log\left(\frac{x}{X_0}\right)\right) \tag{A.1}$$

[Pat+16; Hig75], depending on the radiation length $X_0$ and the material thickness $x$. $\beta c$ is the particle's velocity and $z$ its charge number. For low momenta $p$ the scattering effects are larger.

For a detector with four layers spaced in pairs of two with the distance between the second and third layer $\Delta r_{2,3}$ being much larger than the distances between the outer layers $\Delta r_{2,3} \gg \Delta r_{1,2} \approx \Delta r_{3,4}$, the momentum resolution $\sigma_p$ is given by [Sch14a]

$$\frac{\sigma_p}{p} \approx \sqrt{2} \frac{b}{B \cdot s}. \tag{A.2}$$

$b$ is an effective scattering parameter, defined through the Highland formula as

$$b = 13.6\,\mathrm{MeV}/cz\sqrt{\frac{x}{X_0}}\left(1 + 0.038\log\left(\frac{x}{X_0}\right)\right), \tag{A.3}$$

$s$ is the trajectory length, and $B$ the magnetic field.

## A.3. Elevation Angle Cut

For the development of the 5- and 7-hit track reconstruction, loopers are eliminated, as they constitute a large amount of background. The easiest way to do this, is to require a minimum for the elevation angle $\lambda_1$ of the particle's momentum at the first hit. Figure A.2 shows the distribution of true tracks from the first loop and the distribution of fake or sequential tracks for 5- and 7-hit tracks. It is clear from the sharp peak of the latter around $\lambda_1 = 0$ that requiring a minimum for $\lambda_1$ results in a large reduction in background but also eliminates many true tracks.

A value for this cut can be chosen by the same method described in chapter 7.1.1, using efficiency and purity, but requiring a track to be true and correspond to the first loop to count as signal. Everything else is background. The cut value is found to be optimal at $\lambda_{\mathrm{cut}} = 0.14$ resulting in a background reduction by $R = 67\,\%$ while losing $20\,\%$ of signal tracks at a purity of $P = 66\,\%$, see figure A.3.

This cut was only applied during the development and is not in place for the studies presented in this thesis.

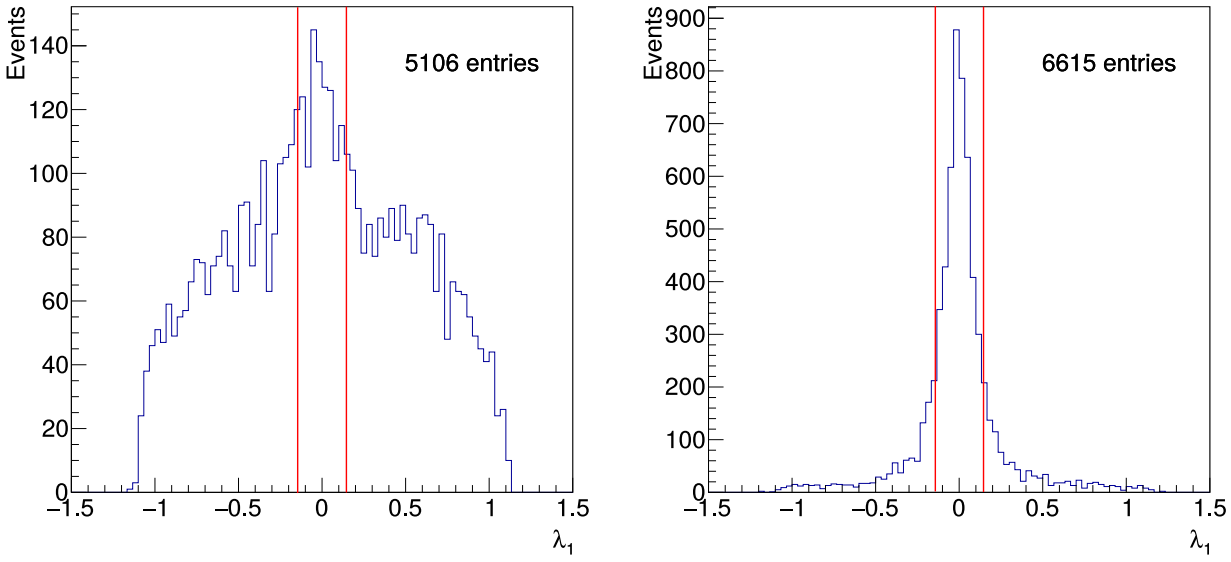


**(a)** Elevation angle $\lambda_1$ of the particle's momentum at the first hit for 5- and 7-hit tracks in the first loop.

**(b)** $\lambda_1$ for tracks that do not correspond to a particle's first loop and fake tracks.

**Figure A.2.:** Analyzing the elevation angle $\lambda_1$ of the particle's momentum at the first hit for 5- and 7-hit tracks shows that fake tracks and tracks not corresponding to a particles first loop are dominantly transverse. Requiring a minimum for $|\lambda_1|$ eliminates a lot of loopers. The red lines indicate the chosen value for $|\lambda_{1,\mathrm{min}}| = 0.14$.

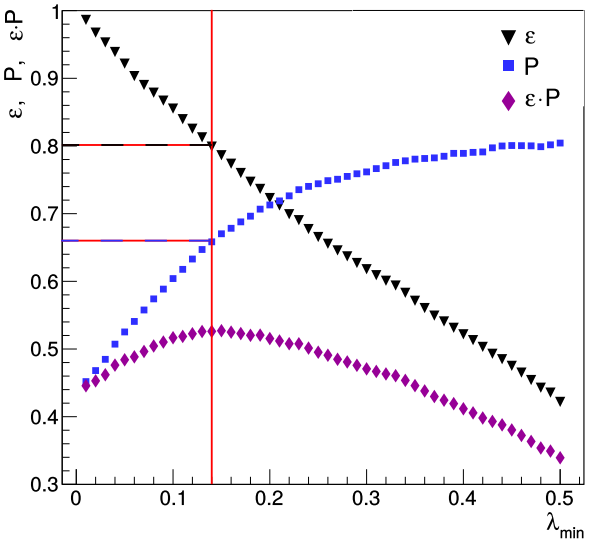


**(a)** Analysis of signal efficiency $\varepsilon(\lambda_{\text{min}})$ (blue) and purity $P(\lambda_{\text{min}})$ (yellow) for different cuts on $\lambda_{\text{min}}$ between 0 and 0.5. The cut is set at $\lambda_{\text{cut}} = 0.14$ resulting in a purity of $P = 66\,\%$ while losing 20 % of signal tracks.

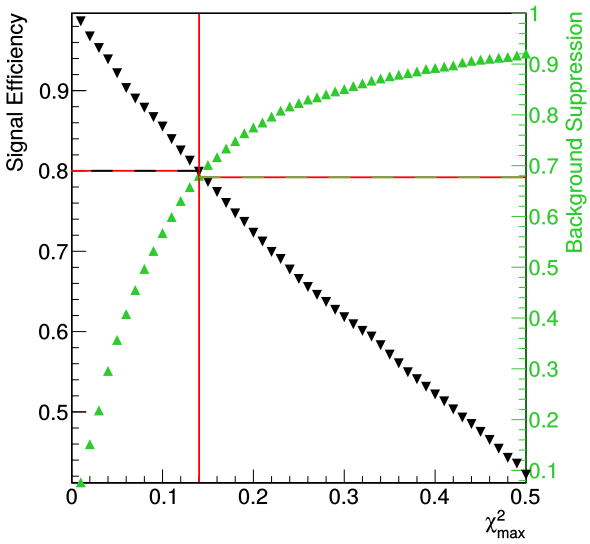


**(b)** The chosen cut at $\lambda_{\text{cut}} = 0.14$ reduces the background tracks by $R = 67\,\%$.

**Figure A.3.:** Placing a cut on the elevation angle $\lambda_1$ of the particle's momentum at the first hit. Signal tracks include only true tracks corresponding to a particle's first loop. This is conducted with a data set containing $10^4$ reconstructed 5- and 7-hit tracks with the $\chi^2$ cuts chosen above.

## A.4. $\chi^2$ Distributions

The number of degrees of freedom, ndf, is given by the number of triplets forming a track:

$$\text{ndf} = 2 \cdot \#\text{ of triplets} - 1 \tag{A.4}$$

$$\#\text{ of triplets} = \#\text{ of hits} - 2. \tag{A.5}$$

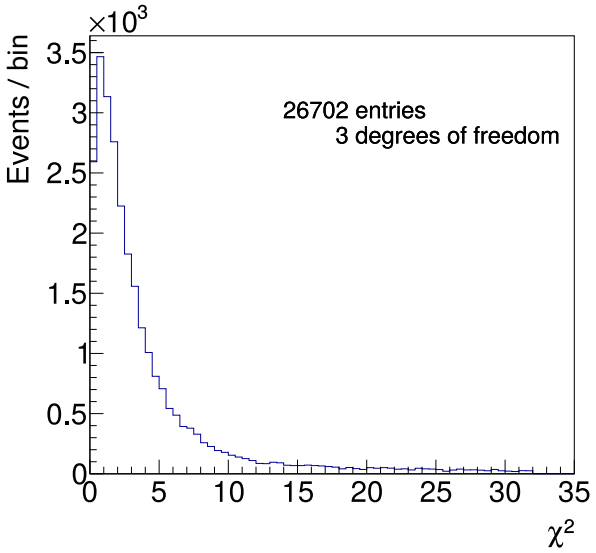


**Figure A.4.:** $\chi^2$ distribution for 4-hit tracks. The cut at $\chi^2 = 32$ results in 89 % true tracks with an efficiency of over 99 %.

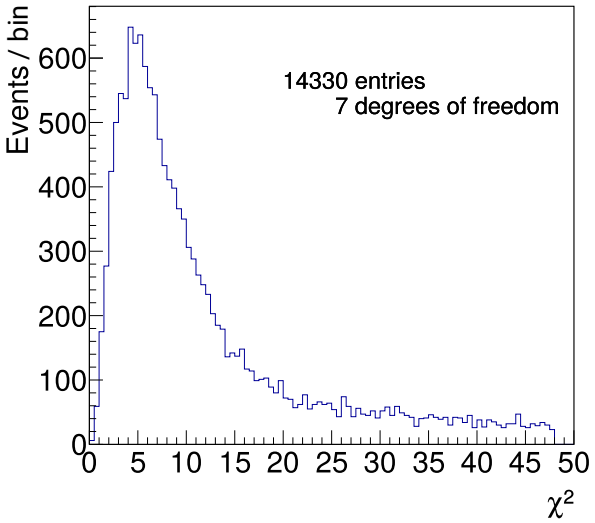


**(a)** $\chi^2$ distribution for 6-hit tracks. The cut at $\chi^2 = 48$ results in 77 % true tracks with an efficiency of over 99 %.

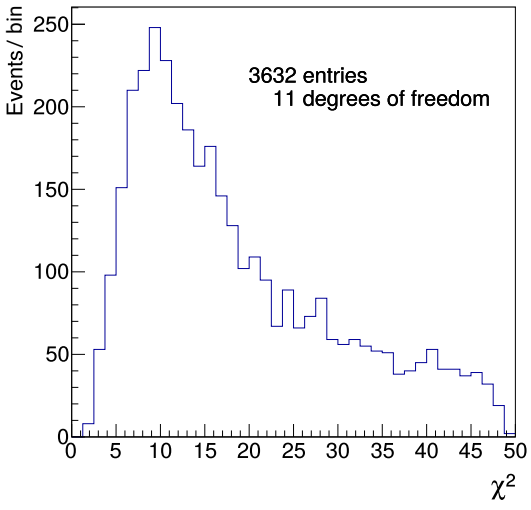


**(b)** $\chi^2$ distribution for 8-hit tracks. The cut at $\chi^2 = 48$ results in 68 % true tracks with an efficiency of 97 %.

**Figure A.5.:** $\chi^2$ distribution for tracks reconstructed with the standard reconstruction.

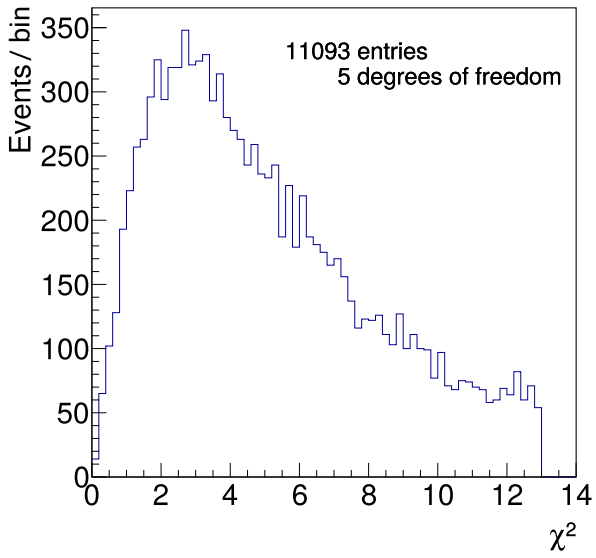


**(a)** $\chi^2$ distribution for 5-hit tracks. The cut at $\chi^2 = 13$ results in 71 % true tracks with an efficiency of 93 %.

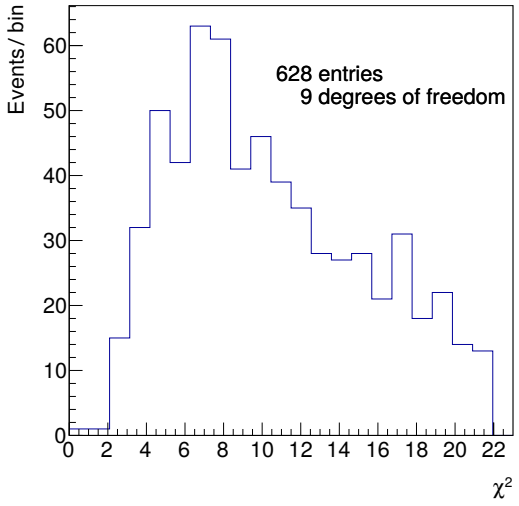


**(b)** $\chi^2$ distribution for 7-hit tracks. The cut at $\chi^2 = 22$ results in 70 % true tracks with an efficiency of over 87 %.

**Figure A.6.:** $\chi^2$ distribution for tracks without a hit in the first pixel layer, reconstructed with the extended track reconstruction.

## A.5. Momentum Distribution

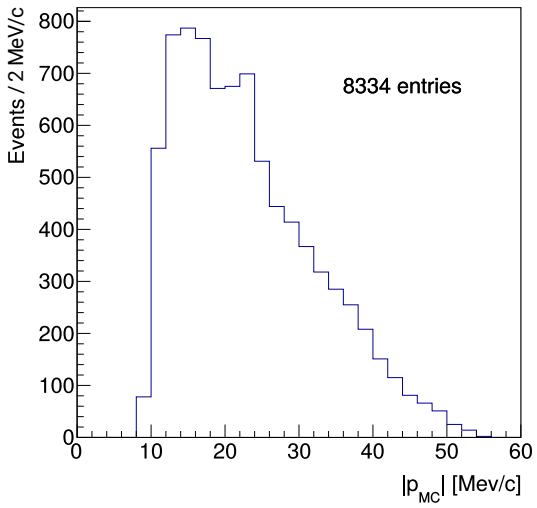


**(a)** True momentum of 5-hit tracks.

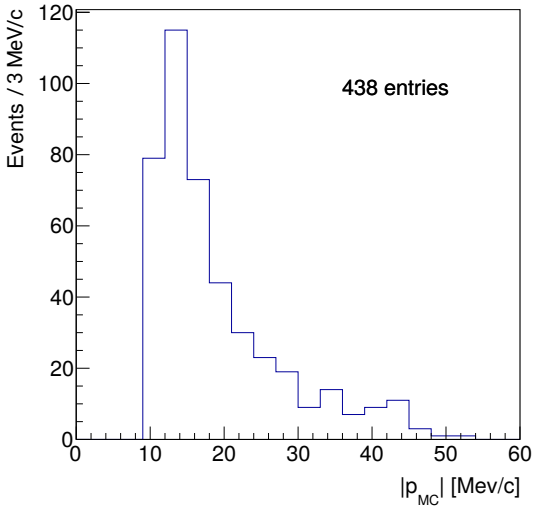


**(b)** True momentum of 7-hit tracks. Only few tracks with high momentum recurl inside the central detector.

**Figure A.7.:** Distribution of absolute track momentum $|p_{\mathrm{MC}}|$.

## A.6. Momentum Resolution

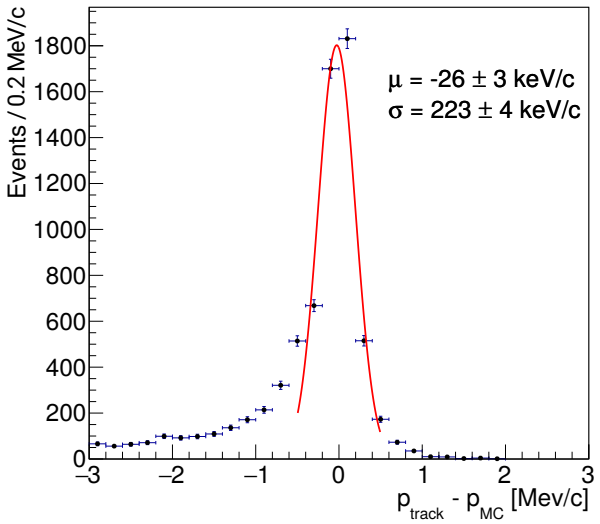


**(a)** The momentum resolution for 5-hit tracks is $\sigma \approx 0.22\,\mathrm{MeV}/c$.

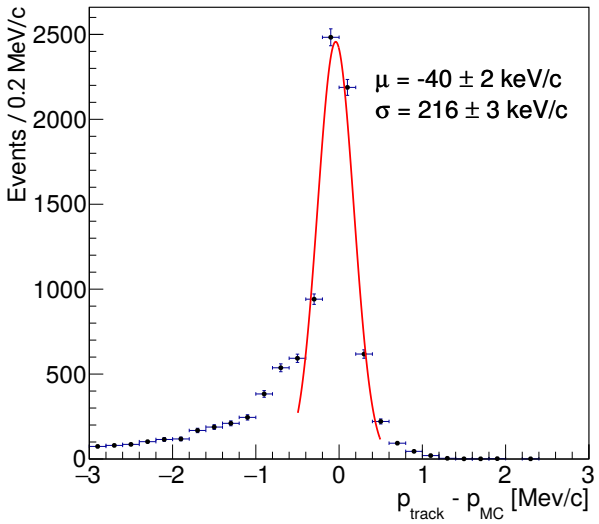


**(b)** The momentum resolution for 6-hit tracks is $\sigma \approx 0.22\,\mathrm{MeV}/c$.

**Figure A.8.:** The difference between the reconstructed momentum $p_{\mathrm{track}}$ and the simulated momentum $p_{\mathrm{MC}}$. The core of the distribution is fitted with a Gaussian, giving the momentum resolution $\sigma$. 5-hit tracks originating in the second layer are compared to 6-hit tracks from within the first layer. Both produce two recurl hits.

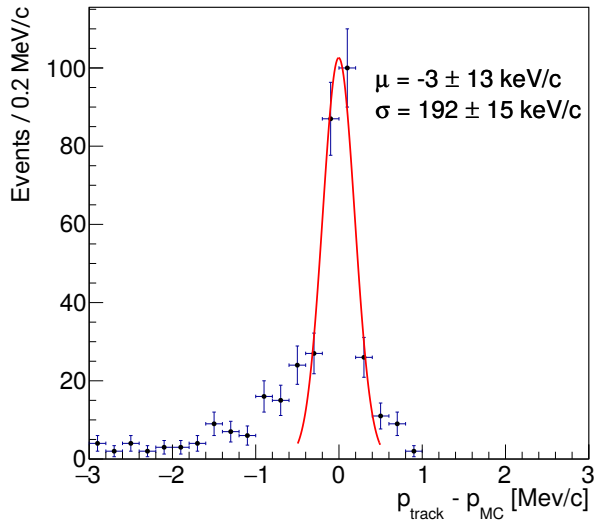


**(a)** The momentum resolution for 7-hit tracks is $\sigma \approx 0.19\,\mathrm{MeV}/c$.

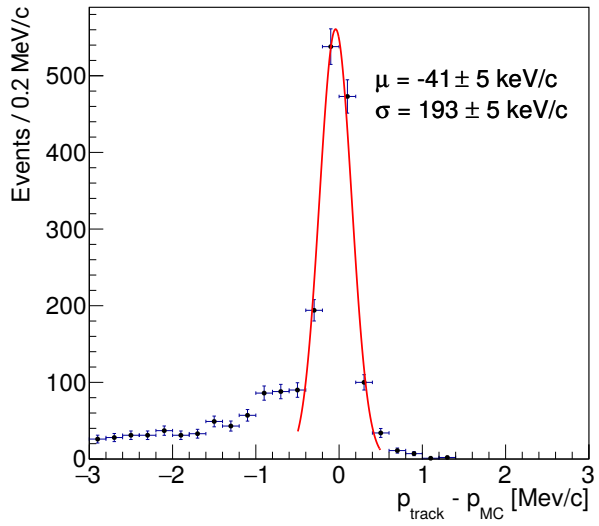


**(b)** The momentum resolution for 8-hit tracks is $\sigma \approx 0.19\,\mathrm{MeV}/c$.

**Figure A.9.:** The difference between the reconstructed momentum $p_{\mathrm{track}}$ and the simulated momentum $p_{\mathrm{MC}}$. The core of the distribution is fitted with a Gaussian, giving the momentum resolution $\sigma$. 7-hit tracks originating in the second layer are compared to 8-hit tracks from within the first layer. Both recurl inside the central detector and produce two hits in the vertex layers.

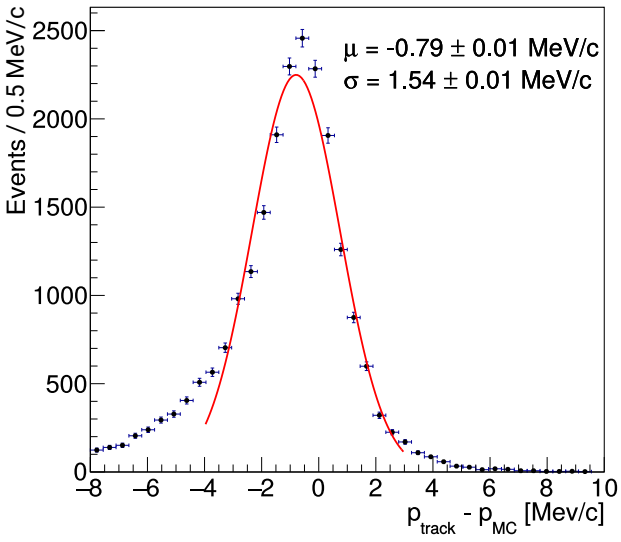


**Figure A.10.:** The difference between the reconstructed momentum $p_{\text{track}}$ and the simulated momentum $p_{\text{MC}}$ for 4-hit tracks. The core of the distribution is fitted with a Gaussian, giving the momentum resolution $\sigma \approx 1.5\,\text{MeV}/c$. This is significantly worse than for long tracks as the tracks have not yet recurled.

## A.7. Material Mapping

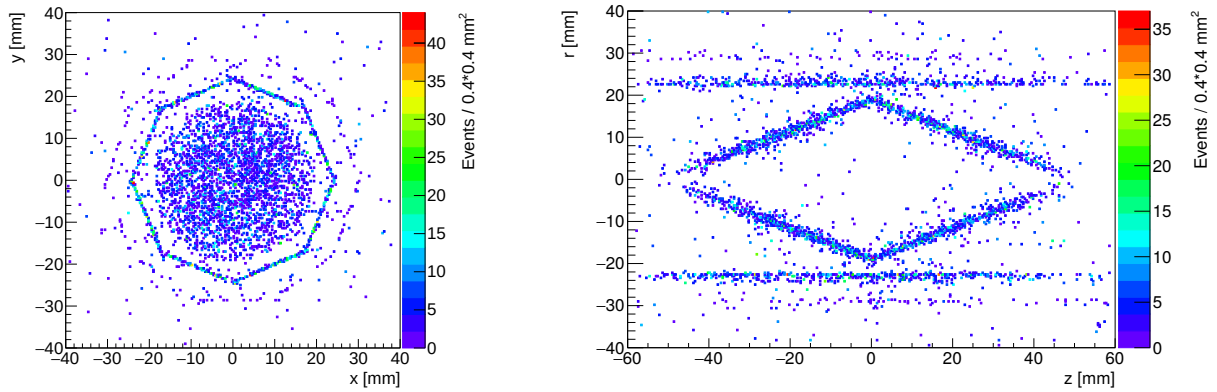


**(a)** Transverse view.

**(b)** Projection onto the $r-z$ plane. Vertices with $y < 0$ are projected onto $-r$.

**Figure A.11.:** The reconstructed vertices of $e^+e^-$ pairs from Bhabha scattering and photon conversion evetns. A cut on the invariant mass at $m_{\text{inv}} = 5\,\text{MeV}/c^2$ reduces the number of Bhabha events by 65 %. Accordingly, the number of vertices from wrong combinations of Bhabha electrons is significantly reduced compared to figure 7.8.

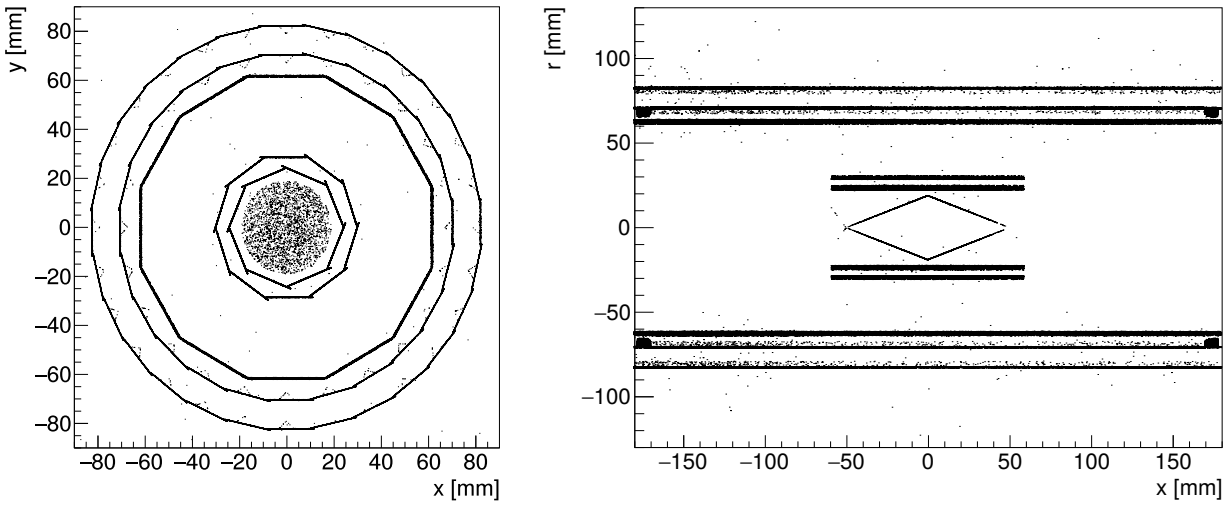


**(a)** Transverse view. The v-shaped folds for support and cooling on the outer pixel layers can be seen.

**(b)** Projection onto the $r$-$z$ plane. Vertices with $y < 0$ are projected onto $-r$. On both ends of the third pixel layer the electrical endpieces can be seen.

**Figure A.12.:** True vertices of all conversion events.

# List of Figures

# List of Tables

# Bibliography


[Ago+03] S. Agostinelli et al. “Geant4 - A simulation toolkit”. In: *Nucl. Instrum. Meth. A* 506.3 (2003). DOI: 10.1016/S0168-9002(03)01368-8.

[Bal+13] A. M. Baldini et al. “MEG Upgrade Proposal”. In: *ArXiv e-print* (2013). (arXiv:1301.7225).

[Bal+16] A. M. Baldini et al. “Search for the lepton flavour violating decay $\mu \to e\gamma$ with the full dataset of the MEG experiment”. In: *Eur. Phys. J. C76* 8 (2016), p. 434. DOI: https://doi.org/10.1140/epjc/s10052-016-4271-x.

[Bar+95] R. Barbieri et al. “Violations of lepton flavour and CP in supersymmetric unified theories”. In: *Nuclear Physics B* 445, 2-3 (1995), pp. 219–251. DOI: 10.1016/0550-3213(95)00208-A.

[Bas+81] B. Bassalleck et al. “The observation of charge exchange of pions captured in several nuclei”. In: *Nucl. Phys. A* 362.2 (1981). DOI: 10.1016/0375-9474(81)90504-2.

[Bat+09] B. Batell et al. “Exploring portals to a hidden sector through fixed targets”. In: *Phys. Rev. D* 80.095024 (2009). DOI: 10.1103/PhysRevD.80.095024.

[Bat15] J. R. Batley. “Search for the Dark Photon in $\pi^0$ decays”. In: *Physics Letters B* 746 (2015), pp. 178–185. DOI: 10.1016/j.physletb.2015.04.068.

[Bau17] M. Bauer. *Dark Photons and the Invisible Sector*. Talk at the *Mu3e* collaboration meeting. 2017.

[Bel+88] U. Bellgardt et al. “Search for the decay $\mu^+ \to e^+e^+e^-$”. In: *Nuclear Physics B* 299.1 (1988), pp. 1–6. ISSN: 0550-3213. DOI: http://dx.doi.org/10.1016/0550-3213(88)90462-2.

[Ber+14] N. Berger et al. “Multiple Coulomb Scattering in Thin Silicon”. In: *JINST* 9 (2014). DOI: 10.1088/1748-0221/9/07/P07007.

[Ber+17] N. Berger et al. "A New Three-Dimensional Track Fit with Multiple Scattering". In: *Nucl. Instrum. Meth. A* 844 (2017), pp. 135–140. ISSN: 0168-9002. DOI: 10.1016/j.nima.2016.11.012. (arXiv:1606.04990 [physics.ins-det]).

[Ber17] N. Berger. *Physics with Pions*. Talk at the *Mu3e* collaboration meeting. 2017.

[Bij+16] J. Bijnens et al. "Pion light-by-light contributions to the muon $g-2$". In: *JHEP* 1609 (2016). DOI: 10.1007/JHEP09(2016)113. (arXiv:1608.01454 [hep-ph]).

[Blo+13] A. Blondel et al. "Research Proposal for an Experiment to Search for the Decay $\mu \to eee$". In: *ArXiv e-prints* (2013). (arxiv:1301.6113).

[Blo+16a] A. Blondel et al. *Mu3e Experiment: Phase I*. Supporting Document. Jan. 2016.

[Blo+16b] A. Blondel et al. *Mu3e Experiment: Technical Design of the Phase I*. Dec. 2016. to be published.

[Bu+08] J. Bu et al. "Lepton flavor violating muon decays in a model of electroweak-scale right-handed neutrinos". In: *Physics Letters B* 665, 1 (2008), pp. 39–43. DOI: 10.1016/j.physletb.2008.05.059. (arXiv:0802.3241 [hep-ph]).

[Cen16] P. Cenci. "The neutral pion form factor at NA62". In: *J. Phys.: Conf. Ser.* 770.1 (2016). DOI: 10.1088/1742-6596/770/1/012035.

[Che+13] C. Cheng et al. "The next generation of $\mu \to e\gamma$ and $\mu \to 3e$ CLFV search experiments". In: *ArXiv e-prints* (2013). (arXiv:1309.7679 [physics.ins-det]).

[Dji+09] R. M. Djilkibaev et al. "Rare Muon Decay $\mu^+ \to e^+e^-e^+\nu_e\overline{\nu}_\mu$". In: *Phys.Rev. D* 79 (2009). DOI: 10.1103/PhysRevD.79.073004.

[Ech+15] B. Echenard et al. "Projections for Dark Photon Searches at Mu3e". In: *JHEP* 1501 (2015). DOI: 10.1007/JHEP01(2015)113. (arXiv:1411.1770 [hep-ph]).

[Eid16] S. Eidelman. *Muon (g-2)/2 and Transition Form Factors*. Talk at the Particle Colloquium. Physikalisches Institut, Universität Heidelberg, 2016.

[Ess+13] R. Essig et al. "Dark Sectors and New, Light, Weakly-Coupled Particles". In: *ArXiv e-prints* (2013). (arXiv:1311.0029).

[For97] F. Foroughi. *$\pi E1$ Secondary Beam Line*. 1997. URL: http://aea.web.psi.ch/beam2lines/pie1.pdf.

[Fuk+98] Y. Fukuda et al. "Evidence for Oscillation of Atmospheric Neutrinos". In: *Phys. Rev. Lett.* 81 (1998), pp. 1562–1567. DOI: 10.1103/PhysRevLett.81.1562. (arXiv:hep-ex/9807003).

[Ger17] L. Gerritzen. "Reconstruction of Two-Prong Signatures with a Linearised Multiple Scattering Vertex Fit for Mu3e". Master Thesis. Physikalisches Institut der Universität Heidelberg, 2017.

[GS08] C. Grupen and B. Shwartz. *Particle Detectors*. 2nd edition. Cambridge University Press, 2008. ISBN: 978-0-521-84006-4.

[Hig75] V. L. Highland. "Some Practical Remarks on Multiple Scattering". In: *Nucl. Instrum. Meth. A* 129.2 (1975), pp. 497–499. DOI: 10.1016/0029-554X(75)90743-0.

[KS16] M. Kiehn and S. Schenk. *Scattering Vertex Fit Notes*. Internal Note. 2016.

[M L17] Private communications with M. Lubej. 14.03.2017. URL: http://www-f9.ijs.si/~lubej/SM.pdf.

[Mih+13] S. Mihara et al. "Charged Lepton Flavor-Violation Experiments". In: *Ann. Rev. Nucl. Part. Sci.* 63 (2013), pp. 531–552. DOI: 10.1146/annurev-nucl-102912-144530.

[Mur02] B. Murakami. "The Impact of lepton flavor violating Z-prime bosons on muon g-2 and other muon observables". In: *Phys. Rev. D* 65 (2002). DOI: 10.1103/PhysRevD.65.055003.

[Pap17] A. Papa. *Dark Photon search via pion decays with Mu3e*. Talk at the *Mu3e* collaboration meeting. 2017.

[Pat+16] C. Patrignani et al. *Review of Particle Physics*. 2016. DOI: 10.1088/1674-1137/40/10/100001.

[Per07] I. Perić. "A novel monolithic pixelated particle detector implemented in high-voltage CMOS technology". In: *Nucl. Instrum. Meth. A* 582 (2007). DOI: 10.1016/j.nima.2007.07.115.

[Per14] A. K. Perrevoort. "Sensitivity Studies and Front-End Firmware for the Mu3e Experiment". Doctoral Thesis. Physikalisches Institut der Universität Heidelberg, started 2014.

[Sch12] S. Schenk. "A Vertex Fit for Low Momentum Particles in a Solenoidal Magnetic Field with Multiple Scattering". Bachelor Thesis. Physikalisches Institut der Universität Heidelberg, 2012.

[Sch13] A. Schöning. *Linearised Vertex 3D Fit in a Solenoidal Magnetic Field with Multiple Scattering*. Internal Note. 2013.

[Sch14a] A. Schöning. *Track Fit with Multiple Scattering*. Internal Note. 2014.

[Sch14b] A. Schöning. *A Three-Dimensional Helix Fit with Multiple Scattering using Hit Triplets*. Internal Note. 2014.

[Sch17] A. Schöning. *Mu3e-gamma*. Talk at the *Mu3e* collaboration meeting. 2017.

[Seg65] E. Segré. *Nuclei and Particles*. New York: W. A. Benjamin, 1965.

[Tho13] M. Thomson. *Modern Particle Physics*. Cambridge, U.K.: Cambridge University Press, 2013. ISBN: 978-1-107-03426-6.

# Acknowledgements

This thesis owes its existence to a great many people and I would like to thank all of them for their support.

Foremost, there is Professor **André Schöning**, who welcomed me to his group without knowing more about me than that I was interested in particle physics and didn't have any experience with programming. I would like to thank him for his confidence and for the generosity in giving me every opportunity to learn about the tools and the topic.

It was an exceptional pleasure to be part of the *Mu3e* group and their uniquely wonderful members for the past year and I have different reasons to be grateful to each of them:

First of all, **Ann-Kathrin**, not only for ensuring the physical fitness of *Mu3e*, but also for being a reliable, caring and inspiring supervisor. Her advice during all stages of my work was invaluable, not in the least during the last two months, while teasing out the maximum amount of content and structure from my work. I trust her opinion implicitly.

Secondly, **Lukas**, my fellow Master student, to whom I owe most of my sanity (and many episodes of insanity). Although we were, in fact, working on different projects, I hugely benefited from his superior computer skills and his willingness to help and discuss anything. Aside from that, I can only say that even though he is easily damaged and unaffected by penetrating stares, I would not have enjoyed this time half as much without him.

**Alex**, in Mainz, whose creation I had the honor to work with. I want to thank him for answering every single one of my questions and helping me with solid advice whenever I was stuck. His coding style is now my standard.

**Simon**, in Zürich, who supplied just the perfect feature right when I needed it and was always available with help and explanations. His proofreading comments were as sweet as they were helpful.

**Nik**, for organizing our weekly software meeting, that reminded me on a regular basis that there is more than hardware to an experiment.

**Dirk**, who is The Hand, the grey eminence, who oversees everything. Thank you for your support and for understanding the need to travel.

**Lennart**, who got up when I couldn't and never spoke of it again. My first thoughts are of him, whenever my computer breaks, and it is he, who taught me plotting. His contributions to the social exploits of this group are invaluable.

**Heiko**, who has the most infectious grin and deserves nothing but admiration for dealing so bravely with his disabling nut problem.

**Jens**, who checked and rechecked this thesis for every missing comma without collecting his bribe.

**Sebastian**, whose serene presence hides a taste for extraordinarily bad jokes.

**Lars**, for making those jokes.

**Adrian**, for being the most unobtrusive office mate one could imagine. There is no one I would rather have sitting in my back.

**Tamasi**, who adds exotic flavor to *Mu3e*.

**David**, for Haribo, countless barbecues and reminding me to write.

**Jan**, for his unique presence, knowing everything and making me feel included.

And to all the other members of *Mu3e* for providing a very special working environment. There aren't enough cakes to express my gratitude to all of you.

Erklärung:

Ich versichere, dass ich diese Arbeit selbstständig verfasst habe und keine anderen als die angegebenen Quellen und Hilfsmittel benutzt habe.

Heidelberg, den 18.04.2017 .....